ELSEVIER

Contents lists available at ScienceDirect

## Additive Manufacturing

journal homepage: www.elsevier.com/locate/addma





# Exploring spatial beam shaping in laser powder bed fusion: High-fidelity simulation and in-situ monitoring

Mohamad Bayat <sup>a,f,\*</sup>, Richard Rothfelder <sup>b,c,f</sup>, Karen Schwarzkopf <sup>b,c,f</sup>, Aleksandr Zinoviev <sup>f,g</sup>, Olga Zinovieva <sup>f,g</sup>, Christoph Spurk <sup>c,f</sup>, Mark Hummel <sup>d,e,f</sup>, Alexander Olowinsky <sup>d,f</sup>, Felix Beckmann <sup>e,f</sup>, Julian Moosmann <sup>e,f</sup>, Michael Schmidt <sup>b,c,f</sup>, Jesper H. Hattel <sup>a,f</sup>

- <sup>a</sup> Department of Mechanical Engineering, Technical University of Denmark (DTU), Building 425, Kgs. Lyngby 2800, Denmark
- b Lehrstuhl für Photonische Technologien (LPT, Prof. Schmidt), Friedrich-Alexander-Universität Erlangen-Nürnberg, Konrad-Zuse-Straße 3/5, Erlangen 91052, Germany
- <sup>c</sup> Graduate School in Advanced Optical Technologies (SAOT), Paul-Gordan-Straße 6, Erlangen 91052, Denmark
- d RWTH Aachen University, Chair for Laser Technology LLT, Steinbachstraße 15, Aachen 52074, Germany
- e Fraunhofer-Institute for Laser Technology ILT, Steinbachstraße 15, Aachen 52074, Germany
- f Institute of Materials Physics, Helmholtz-Zentrum Hereon, Max-Planck-Str. 1, Geesthacht 21502, Germany
- g School of Engineering and Technology, UNSW Canberra, University of New South Wales, Northcott Dr., Campbell, ACT 2612, Australia

#### ARTICLE INFO

# Keywords: Beam shaping Ring-spot beam shape Laser powder bed fusion In-situ monitoring Multiphysics simulation Microstructure modeling

#### ABSTRACT

Laser beam shaping is a novel and relatively unexplored method for controlling the melt pool conditions during metal additive manufacturing (MAM) processes, but even so it still holds good promise for achieving site-specific tailored properties. In this work, a comprehensive numerical and experimental campaign is carried out to explore this subject within metal laser powder bed fusion (LPBF). More specifically, a multiphysics numerical model is implemented for simulating the heat and fluid flow conditions during LPBF of Ti6Al4V using arbitrary circular beam shapes with various power distributions spanning from a pure Gaussian beam to a pure ring beam profile. The model is subsequently coupled with cellular automata to describe the beam shape effects on the microstructure evolution. Model validation is carried out in a two-fold manner. First, we compare the predicted melt pool cross-section with the one from ex-situ single track experiments, and we find a deviation of less than 9 % in melt pool dimensions. Secondly, advanced in-situ X-ray monitoring is carried out to unravel the melt pool dynamics and we find that the predicted morphology closely matches the in-situ X-ray results. Moreover, it is shown that at lower laser power, a bulge of liquid metal forms at the center of the melt pool when employing ring profiles, and this is ascribed to the absence of recoil pressure at the center of the ring beam. Furthermore, increasing the laser power seems to destabilize the melt pool regime, as the central bulge transforms into a liquid metal jet that periodically collapses and breaks up into hot spatter. Based on the results, we believe that our multiphysics modelling methodology, opens up new pathways for predicting how laser beam shaping influences porosity, surface roughness as well as microstructure formation in LPBF processes.

#### 1. Introduction

Variation of input process parameters for achieving a part with sound quality has been widely investigated over the past couple of years in MAM processes [1–3]. Laser power, scanning speed, scanning pattern, laser beam diameter and powder layer thickness are on top of the list when it comes to process optimization targeting maximum part density, which is most frequently defined as the primary quality criterion in MAM. Comparatively, fairly little attention has been paid to beam

shaping (BS), an emerging technology that allows for controlling the laser's spatio-temporal intensity variation. As BS allows for localized control of the laser's power intensity during manufacturing, it is potentially the most suitable choice for triggering site-specific microstructural manipulation or density control of a part [4].

BS can be carried out and applied to MAM processes both temporally and spatially. Temporal BS (T-BS) refers to time-wise modulation of the laser beam intensity over the course of manufacturing. This is typically done in two ways, point-wise control, or continuous modulation of the

https://doi.org/10.1016/j.addma.2024.104420

<sup>\*</sup> Correspondence to: Department of Civil and Mechanical Engineering, Technical University of Denmark (DTU), Building 425, Kgs. Lyngby 2800, Denmark. E-mail address: mbayat@mek.dtu.dk (M. Bayat).

laser power. In point-wise control, two input parameters, namely the point-wise distance and the on-time duration or the dwelling time are defined, dictating in essence how far the laser is allowed to move within each step and for how long the laser is supposed to irradiate the target surface. Numerical simulations are one of the most useful tools for studying the influence of process conditions in LPBF. Among the three major modelling types introduced in [5], namely micro-scale, deposition-scale and part-scale models, deposition-scale simulations are the most suitable option for studying the detailed melt pool behavior within the deposition site i.e. the laser irradiation zone in LPBF. Zheng et al. [6] did a computational fluid dynamics (CFD) simulation at deposition-scale of the point-wise modulated LPBF process of the In625 alloy. They noticed that fish-fin-like meso-features form at the wake of the melt pool due to repeated variation in the recoil pressure caused by successive on-and-off cycles of the laser beam. Plotkowski et al. [7] and Raghavan et al. [8] implemented a relatively similar strategy to control the input power in LPBF and electron beam PBF, and they simulated the melt pool using pure conduction heat transfer models. In the latter type of T-BS, i. e. continuous modulation, sequential on-and-off cycles of the moving laser beam take place over a cycle period – a time period over which an entire on-and-off cycle takes place. This parameter together with the duty cycle determines the melt pool shape. The duty cycle is given in percentage and it specifies the fraction of the laser's on-time duration to the entire cycle period [9]. Along this line, Bayat et al. [10] studied the impact of cycle period as well as duty cycle on the melt pool conditions along with the solidified track's surface morphology for LPBF of stainless steel 316-L and they noted significant congestion of fish-fin surface topologies at lower cycle periods. As of now, the bulk of the simulation efforts in LPBF have been dedicated to ordinary process parameter variation, hence simulation of T-BS is quite scarce in the literature devoted to modelling of LPBF.

BS has several unique advantages, one of which is that the more widely used Gaussian beam profile (GBP), due to the very high laser heat flux concentration, could lead to excessive evaporation or unwanted ablation of the material, leading to hot spatter formation and this can be alleviated via employing BS. Further melt pool control and manipulation of the resultant microstructure in MAM is another major proven advantage of BS [11,12]. In the case of wire-based directed energy deposition (DED), any shadowing of the feedstock material could prevent the baseplate from being properly warmed up [13] and this could be a potential space for employing BS to go around the feedstock shadowing effect. In two recent studies, it was demonstrated that the spatter formation and the subsequent feedstock contamination in LPBF are reduced substantially when switching the laser beam profile from the GBP to an annular or ring beam shape [14,15]. It is also shown that using ring beam shapes with wider coverage areas instead of the GBP can result in boosted productivity in LPBF, but this is highly dependent on other process parameters as well [16]. In this respect, variation of the laser beam profile can be beneficial for achieving both productivity increase and quality improvement. Spatial BS (S-BS), as its name implies, can change the focused beam's intensity distribution. Two widely-used S-BS techniques are the adjustable ring mode (ARM) technique and the implementation of adaptive optical elements (AOE). ARM exploits the addition of multiple laser beam profiles e.g. a ring and a Gaussian beam and in this way it induces a wide variety of beam profiles (BPs) [17,18], whereas in the AOE method, one can modify the focused beam's intensity distribution by introducing an opposite aberration to the focused beam's phase aberration by utilizing AOEs right before the optical lens [19,20].

Delving deeper, S-BS can be subdivided into uncontrolled and controlled S-BS. A remarkable instance of the former type is when the laser beam's inclination angle deviates from the targeted vertical direction. In this case, the spatial distribution of the laser beam will automatically diverge from its circular Gaussian profile and consequently form an elliptical shape. This would trigger a scenario in which the beam intensity drops, as the laser's footprint increases while the

laser power remains constant. On the other hand, since the beam's projected area on the sample is elongated, the laser's interaction time with the part is partially prolonged and these two phenomena pose to be working against each other with respect to the overall laser heat input [21,22]. However, the precise impact of the beam's inclination angle, due to the aforementioned complex interplay of prolonged interaction time and expanded projected area, is still unclear. Several research works suggest that increasing the inclination angle could bring about parts with lower density or increased surface roughness [23,24]. Fathi-Hafshejani [25] observed substantial beam profile elongation by measuring the size of the laser's footprint during static pulsed LPBF of AlSi10Mg. They could furthermore notice a clear correlation between the increase in the beam size and the drop in the melt pool depth as a cause of the beam's footprint expansion, for constant input power. They estimated that the laser beam's intensity drops by 6 % when the beam inclination angle is 20°. Li et al. [26] developed a deposition-scale simulation of the LPBF process of a titanium-based alloy and could corroborate the decline of melt pool depth as a function of the laser beam's incidence angle as well.

In contradistinction to such uncontrolled S-BS, where the beam shape is increasingly deformed towards the farther corners of the base plate in LPBF, in controlled S-BS it is possible to manipulate the beam profile's intensity distribution without changing the inclination angle. In this vein, several studies have been performed at the Lawrence Livermore National Laboratory on the role of elliptical beam shapes with two different orientations (transverse and longitudinal) on the metallurgical or morphological conditions of parts printed with LPBF. Matthews et al. [27,28] compared the influence of GBPs and elliptical profiles on the resulting microstructure and concluded that the latter leads to increased levels of equiaxed grains - forging the path for tailored microstructural or morphological conditions. Shi et al. [29] from the same research institute carried out an advanced numerical simulation of the microstructural growth and nucleation with the cellular automata method coupled with their in-house deposition-scale model ALE3D. They found out that depending on the orientation of the elliptical beam, one can obtain totally different grain morphologies than the ones achieved with GBPs. Thereby if the elliptical beam is transversely oriented (with the longer axis perpendicular to the scanning direction), the frequency of appearance of equiaxed grains is promoted - mainly due to lower temperature gradients which are beneficial to nucleation. Roehling et al. [4, 30] concluded that via using a transversely elliptical beam, it is possible to reduce the average grain size up to 50 % as compared to GBPs and this is very advantageous for producing parts without mechanical anisotropy caused by directional grain growth.

Apart from GBPs and elliptical beam shapes or similar closed manifolds (with one single continuous surface area), there exist several beam shapes with open manifolds such as ring-spot beam profiles (RSBP), ring beam profile (RBP), and multiple dots or parallelized beams. Fig. 1 shows different beam shapes with open and closed manifold topologies along with some irregular beam shapes.

Fig. 1(a) and (b) show two instances of typical beam shapes of GBP and RSBP, where the former is categorized as a closed manifold and the latter is an open manifold. Fig. 1(c) and (d) depict beam profiles generated with the CIVAN laser system that is employing coherent beam combination (CBC) [31,32].

Several recent research works have been dedicated to the topic of controlled S-BS and its impact on the build rate, build quality, the build's microstructure and the melt pool's conditions in both laser welding and LPBF. Li et al. [33] simulated two different combinations of ring and circular beams and they showed that a core-to-ring ratio of 5:5 led to a substantially lower keyhole porosity as compared to a pure GBP with a 10:0 ratio and this was above all else ascribed to a larger keyhole opening due to applying a wide ring laser allowing for better bubble escape. Similar observations were reported in [34] where it was shown that the number of keyhole collapses and thus the number of porosities is reduced in laser welding of aluminium 1060 by implementing square or

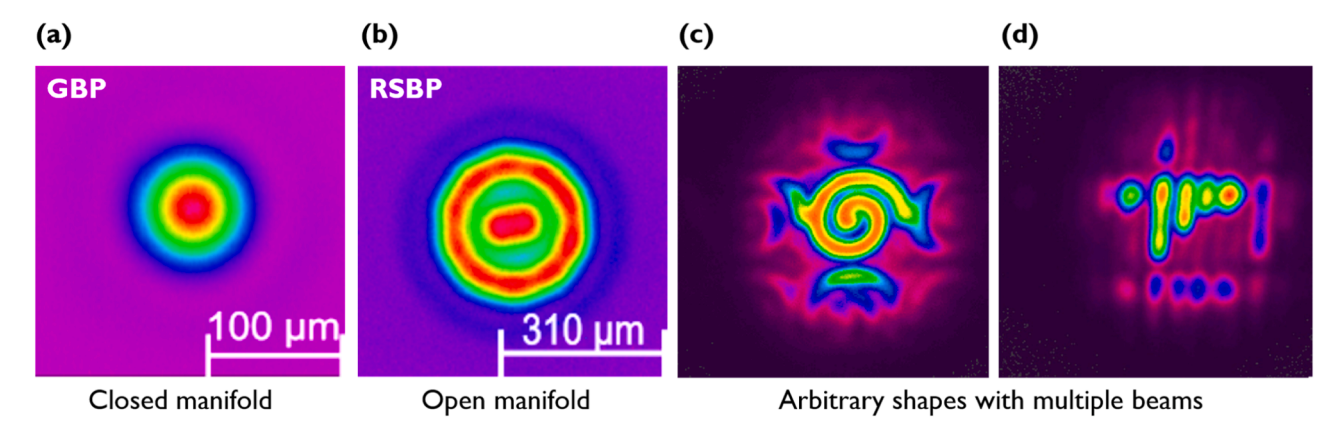


Fig. 1. Some examples of different beam shapes. (a) close manifold: shows the laser heat flux distribution for the GBP. (b) open manifold: shows the RSBP. (a) and (b) are made by the nLight AFX laser system. (c) and (d) are arbitrary beam shapes made with the CIVAN laser system that is based on coherent beam combination (CBC).

elliptical beams shapes. Ebrahimi et al. [35] and Rahimabadi et al. [36] modelled the melt pool dynamics in conduction laser welding with different beam profiles and they could see substantial influence on the melt pool conditions. Rasch et al. [37] studied the effect of ring and line beams on the surface conditions during laser welding of aluminium copper alloys and it was revealed that one can improve the surface roughness value while using RBP. Van Munster et al. [38] printed cubic stainless steel 316-L specimens with three distinct beam profiles of GBP, RBP and mixed beam profile (or RSBP) using the multi-core fiber laser system in their LPBF setup. They showed that even though the RBP improves productivity by 73 %, surface roughness rises by 50 % as compared to GBP. Galbusera et al. [39] tried several combinations of core-to-ring power ratios in LPBF of AlSi7Mg0.6 in the range from 10:0-1:9 and noticed that there was a direct correlation between the ring power's contribution and internal porosities' volume fraction (due to the formation of lack of fusion pores).

Since the beam shaping topic is relatively new within LPBF, only a handful of simulation studies have been specifically directed toward this subject. For instance, Moore et al. [40] recently made an effort to develop a microstructural simulation of the LPBF process of stainless steel 316-L with RBP, RSBP and GBP using the Monte Carlo method. It was reported that smaller and at the same time more equiaxed grains were predicted under RSBP as compared to GBP. However, the thermal model was a simple conduction-based simulation and as concluded in the review paper by Bayat et al. [41] and in the work by Sundqvist [42], a conduction model is far too simplistic for simulating the thermal conditions in LPBF, as several fluid dynamics related physical phenomena occur while running the process. According to [5], the state-of-the-art in the field of LPBF simulations is currently capable of modeling coupled powder and melt pool dynamics conditions [43], multi-material printing [44-46] and even spatter formation [47-50]. However, despite the considerable advancement of deposition-scale simulations, a multiphysics model of the LPBF process with circular core-ring S-BS is currently missing in the literature as pure conduction simulations are not proper representatives of the process physics in LPBF and specifically when accounting for BS [42]. As noted by Tumkur et al. [51], there are very limited efforts done on this subject.

Therefore, in the present work, it is our intention to bridge this gap in the literature and present a multiphysics model validated with experiments carried out both *ex-situ* and *in-situ* to unravel how different circular core-ring beam shapes/modes at different laser power and scanning speeds can affect the melt pool and the subsequent microstructural conditions in LPBF. The rest of the paper is organized as follows; in the next two sections, details of the experimental setups for printing the specimens and description of the numerical model are given. The former also gives an overview of the *in-situ* experiments for monitoring the melt pool under a RBP. The validation of the model is

presented in Section 4 where the input process parameters are listed along with the beam profile's specifications. In the following Section 5, results and discussions are given and the focus is on three pivotal points; (i) the impact of beam shaping with different core-to-ring ratios, (ii) an in-depth analysis of the RBP-induced melt pools predicted by the multiphysics model and (iii) the same captured by the *in-situ* X-ray monitoring setup. The final section of the paper is focused on drawing conclusions and outlining future directions.

#### 2. Experiments

#### 2.1. Single-track experiments

The single weld tracks for validation were created by use of an AFX1000 (nLight, USA) laser integrated into an SLM280hl (Nikon SLM Solutions, Germany) LPBF-machine. The NIR laser has a wavelength of around 1070 nm and is capable of emitting a standard single-mode Gaussian beam profile as well as several multimode beam shapes which are a combination of a ring and a Gaussian beam with different ratios of power distribution. Fig. 2 shows the schematic of the *ex-situ* experiments.

The arrangement of the weld tracks and the corresponding cuts for the cross sections are shown in Fig. 2. Two different power levels of 250 W and 500 W are considered for validation in this work (the tracks marked as "power-capped" were not included in the study). The single track experiments were done with two different beam shapes of GBP and RSBP on two different Ti6Al4V substrates. The scanning speed was fixed to 1 m/s and the approximate beam size for the GBP and RSBP was  $100~\mu m$  and  $350~\mu m$ , respectively. The substrate dimensions are 280~mm by 280~mm and the tracks' length is 225~mm. The focal distance of the lase beam is precisely positioned at the surface of the substrate and the distance is 485~mm. To consider time-dependent effects on weld tracks, five lines with the same line energy were created. All lines were cut, grinded and polished at the same location.

#### 2.2. In-situ online monitoring

The *in-situ* X-ray imaging experiment was conducted in cooperation with Helmholtz-Zentrum Hereon at the German synchrotron facility DESY PETRA III Beamline P07. A fiber laser with adjustable ring mode (Coherent HighLight FL-ARM, Coherent Corp. (USA)) emitting at a central wavelength of 1070 nm was used. The laser system combines two individually controllable laser beams that are coaxially superimposed on the surface of the metal sheet. The laser radiation from both profiles is focused through a lens system consisting of a collimation lens (fc = 70 mm) and a focal lens (ff = 163 mm) on the substrate surface. A metal sheet of 1.4404 (100  $\times$ 30 x 1,5 mm³) is moved underneath the

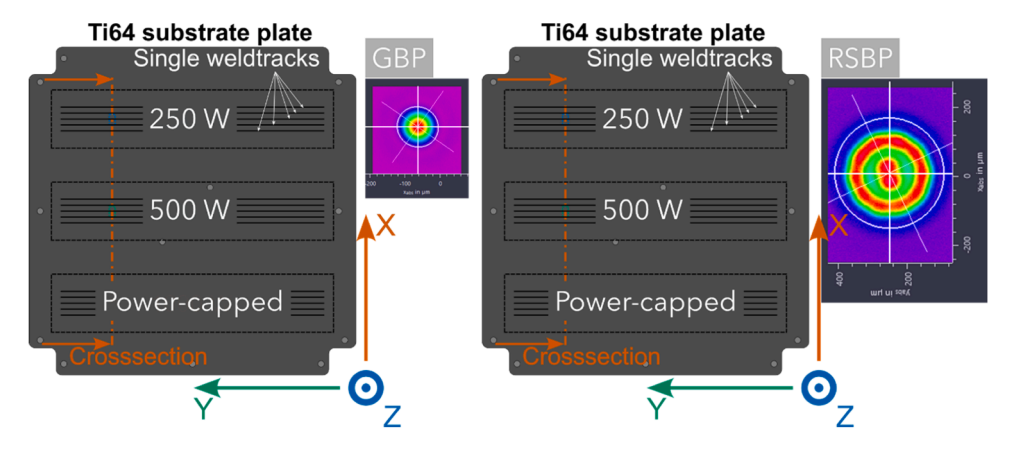


Fig. 2. Schematic top view of the Ti6Al4V substrate plates, which were used for the single weld track experiments. Two identical substrates were used for the single track experiments employing the GBP and RSBP at two laser powers of 250 W and 500 W. "Power-capped" tracks were excluded from the study.

focused laser radiation by means of a linear axis system with a constant velocity of  $500~\text{mm.s}^{-1}$ . To examine the influence of a pure ring intensity distribution, the laser power in the core is set to 0~W and the weld seam track is set to 80~mm.

During the laser beam melting experiment a monochromatic X-ray beam with a photon energy of 73 keV and an approximate diameter of 3 mm transilluminated the metal sample. The X-ray beam is locally attenuated depending on the thickness of the sample. To convert the transmitted X-ray beam to visible light, a scintillator was used which is positioned in front of a high-speed imaging camera operated with a frequency rate of 5 kHz.

#### 3. Numerical models

### 3.1. The deposition-scale model

The multiphysics simulation is developed based on the finite volume method (FVM) and the following conservation equations are solved together to obtain the required field variables in the commercial software package Flow-3D AM module. Detailed descriptions of the physics and equations are given in the previous works of the author group [5,52,53].

$$\frac{\partial \rho \alpha}{\partial t} + \frac{\partial}{\partial x_i} \left( \rho u_j \alpha \right) = \dot{S}_{\alpha}^{"'}, \tag{1}$$

$$\frac{\partial \rho u_i}{\partial t} + \frac{\partial}{\partial x_i} (\rho u_j u_i) = -\frac{\partial p}{\partial x_i} + \mu \nabla^2 u_i - \rho g_i \beta \Delta T - \frac{K_c \left(1 - f_{liq}\right)^2}{C_K + f_{liq}^3} u_i + \dot{S}_u^{"'}, \qquad (2)$$

$$\frac{\partial \rho h}{\partial t} + \frac{\partial}{\partial x_j} \left( \rho u_j h \right) = k \frac{\partial}{\partial x_j} \left( \frac{\partial T}{\partial x_j} \right) + \dot{S}_T^{"'}. \tag{3}$$

Eqs. (1) – (3) stand for mass, linear momentum and energy balance within the computational domain.  $\alpha$  (-) in Eq. (1) is the phase indicator in the volume of fluid (VOF) method and varies between zero and unity expressing void and dense phases, respectively.  $\rho$  (kg.m<sup>-3</sup>) is the density,  $u_i$  (m.s<sup>-1</sup>) is the velocity vector field and p (Pa),  $\mu$  (Pa.s) are the pressure field and dynamic viscosity of the dense phase. The third term on the right hand side of Eq. (2) is buoyancy and  $\beta$  (K<sup>-1</sup>) is the bulk thermal expansion coefficient and the fourth term is related to the solidification drag force.  $f_{liq}$  (-) in Eq. (2) is the liquid fraction function and the other two constants in this term are defined in such a way that the fluid flow is frozen or freed when solidification and melting happens, respectively.  $S_u^{(r)}$  (N.m<sup>-3</sup>) is the source term that contains interfacial forces. T (K), h (J.kg<sup>-1</sup>) and k (W.m<sup>-1</sup>.K<sup>-1</sup>) are temperature field, enthalpy and thermal conductivity, respectively. Enthalpy is a function of temperature as well as the liquid fraction function  $f_{liq}$  (-), and this

function, in the solidification interval, is assumed to linearly increase from zero at  $T_{sol}$  (solidus temperature) and rise to unity at  $T_{liq}$  (liquidus temperature).

$$h(T) = h_0 + \int_{T_0}^T c_p dT + f_{liq} \Delta H_{sl}. \tag{4}$$

Here  $h_0$  (J.kg<sup>-1</sup>) is reference enthalpy and  $\Delta H_{sl}$  (J.kg<sup>-1</sup>) is the latent heat of fusion. The last terms on the right-hand side of Eqs. (1) – (3) express the involved additional physical phenomena in terms of source terms and the implemented source terms are described in Eqs. (5) – (7), respectively [5].

$$\dot{S}_{\alpha}^{"'} = (1 - \theta_r) \sqrt{\frac{M}{2\pi RT}} p_0 \exp\left[\frac{\Delta H_{lv} \bullet M}{R \bullet T_{evap}} \left(\frac{T - T_{evap}}{T}\right)\right] \bullet |\nabla \alpha| \quad D_u,$$
 (5)

$$\dot{S}_{u}^{'''} = \left(0.54 \, p_{0} \exp\left[\frac{\Delta H_{lv} \bullet M}{R \bullet T_{evap}} \left(\frac{T - T_{evap}}{T}\right)\right] + \gamma \left(\nabla T_{i} - n_{i} \left(\nabla T_{j} n_{j}\right)\right) \\
+ \sigma \kappa n_{i} \right) \bullet |\nabla \alpha| \quad D_{u},$$
(6)

$$\dot{\boldsymbol{S}}_{T}^{'''} = \left(\sum \dot{\boldsymbol{Q}}_{RT,k}^{''} + \dot{\boldsymbol{q}}_{conv}^{''} + \dot{\boldsymbol{q}}_{rad}^{''} + \dot{\boldsymbol{S}}_{\alpha}^{'''} \bullet \Delta H_{lv}\right) \bullet |\nabla \alpha| \quad D_{T}. \tag{7}$$

Eqs. (4) – (6) are the implemented source terms for the mass, linear momentum and energy equations, respectively. Eq. (5) stands for the evaporative mass loss. Here  $\theta_r$  (-) is the accommodation coefficient,  $\Delta H_{lv}$  $(J.kg^{-1})$  is the latent heat of evaporation,  $T_{evap}$  (K) is the evaporation temperature, M (kg.Mole<sup>-1</sup>) is the molar mass and R (J.kg<sup>-1</sup>.K<sup>-1</sup>) is the gas constant. Eq. (6) is the source term related to interfacial forces. These three terms in Eq. (6) are only active over a sufficiently thin sublayer (caused by  $|\nabla\alpha|$  ) next to the interface between the dense and gaseous phases. The exponential term expresses the recoil pressure, which acts normally towards the exposed surface of liquid metal, and the middle term expresses thermo-capillarity, while the last term stands for capillarity where  $\kappa$  (m<sup>-1</sup>) is the curvature of the surface. Here  $\sigma$  (N.m<sup>-1</sup>) is surface tension which linearly declines with temperature with the temperature sensitivity coefficient  $\gamma$  (N.m<sup>-1</sup>.K<sup>-1</sup>). The interfacial forces are converted into volumetric forces by means of the continuum surface force (CSF) technique. The two terms  $D_u$  (-) and  $D_T$  (-) in CSF are damping terms which are supposed to put more weight on the dense phase for source distribution over the interface regions. These two terms are described by the following expressions  $D_u = rac{2ar
ho}{
ho_{dense} + 
ho_{gaseous}}$  and  $D_T =$ 

 $\frac{2\overline{c_p\rho}}{\overline{c_p\rho}_{dense}+\overline{c_p\rho}_{gaseous}}$ . Furthermore, in our work, similar to almost all other state-of-the-art works within LPBF simulation, we explicitly describe the recoil pressure. However, some few works tried a sophisticated modelling strategy with a compressible fluid flow assumption to account for the impact of the dense phase's evaporation and expansion and

subsequently its influence on the dense phase's dynamics. Nevertheless, this modelling strategy, even though very accurate and representative of the actual phenomenon, is quite computationally heavy and the results obtained via this method are in very good agreement with the ones determined via implementing the explicit recoil pressure description as an interfacial force [54,55].

The energy source term  $S_T^{\cdots}$  (W.m<sup>-3</sup>) expressed in Eq. (7) involves thermal contributions in the following order;  $\Sigma Q^{\cdots}_{RT,k}$  (W.m<sup>-2</sup>) is sum of all heat flux contributions of every individual discretized laser ray using the ray-tracing method,  $q_{conv}^{\cdots}$  (W.m<sup>-2</sup>) which expresses convection heat flux i.e. Newton's law of cooling,  $q_{rad}$  (W.m<sup>-2</sup>) is the radiation heat flux and finally,  $S_{\alpha}^{\cdots} \Delta H_{lv}$  (W.m<sup>-2</sup>) is the evaporation heat flux, respectively. The laser heat flux distribution in our study is expressed by Eq. (8) [38]. Ray-tracing (see Eq. (9)) with multiple reflections is implemented to model the laser and material interaction to discretize the heat flux in Eq. (8).

$$\dot{q}_{laser}'' = I \left[ \frac{\eta P}{\pi a^2} e^{-\frac{r^2}{a^2}} \right] + (1 - I) \left[ \frac{\eta P}{4\pi \varpi R r_0} e^{-\frac{(r - R)^2}{r_0^2}} \right], \tag{8}$$

$$V_{i,j+1} = V_{i,j+1} - 2(V_{i,j+1} \bullet n)n.$$
(9)

As seen from Eq. (8), the laser heat flux involves two parts, the first part, which describes the Gaussian beam distribution in the center and the second one which accounts for the ring profile. *I* (-) in Eq. (8) defines the portion of the laser power on the central Gaussian profile and as expected, 1-I (-) consequently expresses the ring contribution. It must be noted that the maximum value for I (-) is unity. The rest of the parameters including R (m), a (m),  $r_0$  (m) and  $\varpi$  (-) are ring radius, Gaussian beam radius, radius of the Gaussian distribution of the ring profile and the parameter for the ring profile, respectively. The two parameters  $r_0$ (m) (see Fig. 3(a)) and  $\varpi$  (-) are obtained in such a way that the power is conserved for both RBP and GBP.  $\varpi$  (-) is in essence a scaling parameter for the heat flux to ensure that identical laser powers are achieved when I is zero (RBP) and unity (GBP), respectively, so that the total power for any linear combinations i.e. RSBP is also conserved. In addition,  $\varpi$  (-) ensures that the maximum heat flux values for the RBP and GBP are equal. In Eq. (8),  $\eta$  (-) and P (W) are laser absorptivity and power,

respectively and we set the former to 0.4 in this study. Fig. 3(a) shows the plot and contours of dimensionless laser heat flux intensity for a number of beam modes. Furthermore, the laser-material interaction follows the cosine function rule, meaning that the absorptivity of the laser is geometry-dependent, and the readers can refer to the previous works of the author group for further information [56].  $V_{i,j+1}$  (-) expressed in Eq. (9) is the laser ray's incident/departure vector and the two indices i and j are the ray's identity and iteration numbers and n (-) is the normal vector to the target surface, [52,57,58]. Time-step size is selected to be adaptive and controlled by stability and convergence with a minimum timestep size of  $10^{-6}$  s. The pressure solver type is GMRES and implicit and the VOF algorithm is based on the splic Lagrangian advection method.

The necessary inputs for describing the laser heat flux distribution in Eq. (8) are shown in Fig. 3(a). Here, seven different beam modes ranging from pure GBP to RBP are displayed. The ratio between the core and ring contribution is represented with (C:R), where the overall sum of C and R must be 6. Thus the GBP is described as (6:0) and RBP as (0:6). Therefore, any other combination of these two beam shapes forms a so-called ring spot beam profile (RSBP). Values for RSBP span from (5:1) to (1:5), as shown in Fig. 3(a). The computational domain used for this study is similar to the previous works of the author group [52,53] and a symmetric boundary condition has been applied on the x-z plane, see Fig. 3 (b). According to this, the overall height of the computational domain is  $550 \mu m$  of which  $400 \mu m$  is filled with the dense phase and the rest of it with the gaseous phase. It must be, nevertheless, underlined that in Flow-3D, the VOF algorithm does not track two phases in the laser AM module and the algorithm tracks the free surface of the dense phase instead. However, a precise description of both phases, namely the dense and the gaseous phase, is not required as long as more special physics such as the mutual coupling between the powder particles' movement and the plume generation are not included in the model. We refer the readers to the comprehensive review paper by the author group for better understanding of different types of deposition-scale modelling strategies [5]. Moreover, a uniform cell size is used in the model and based on earlier research works done by the author group [53], a value of 5 µm is chosen to both ensure proper resolution of the laser beam as well as grid-independence. It must, however, be mentioned that the model can predict liquid break-up for droplets smaller than the cell size

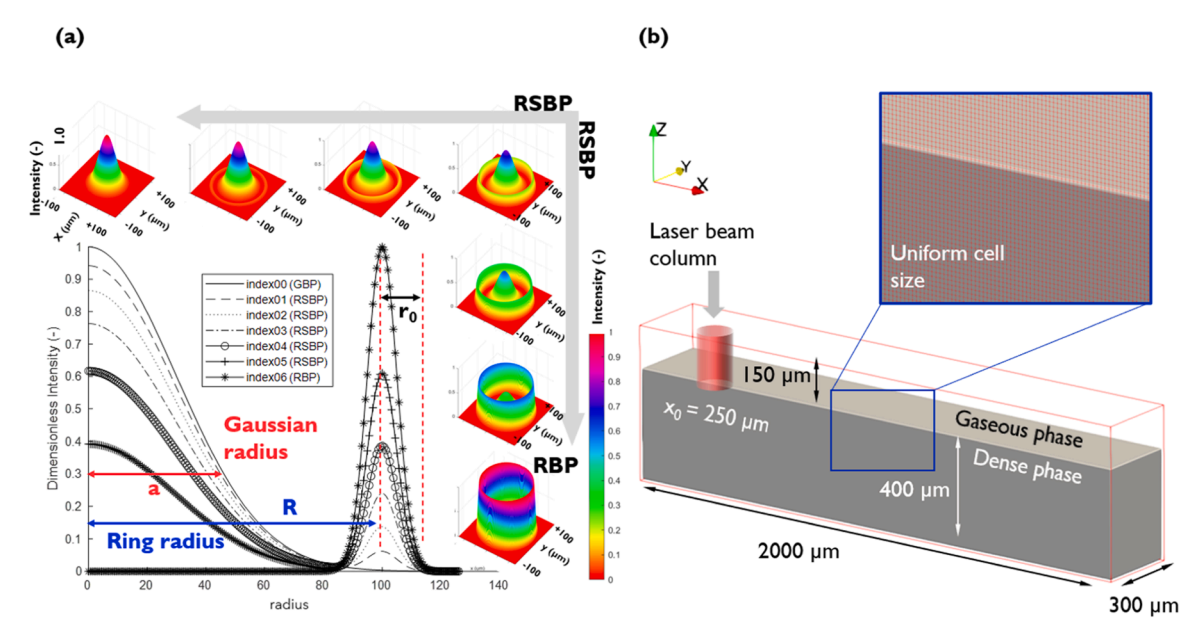


**Fig. 3.** (a) shows the overall laser beam intensity distribution for seven different beam modes ranging from GBP to RBP. Parameters a (m), R (m) and  $r_0$  (m) stand for the Gaussian radius of the center of the beam, the ring radius and the Gaussian radius of the ring, respectively. The contours and the plot show the dimensionless laser heat flux distribution. (b) a 3D view of the computational domain.

as the software has a minimum threshold value of 5 % fill ratio of a cell. However, it is worthwhile to mention that these predictions cannot be fully trusted in case the cell fill ratio is that low i.e. 5-10 % and in such a case finer mesh sizes would be needed The material is selected to be Ti6Al4V and the thermophysical properties are extracted from Flow-3D's material database in addition to some other parameters used in the previous works of the author group [52,59].

#### 3.2. The microstructural model

To describe the beam shaping effects on the microstructure evolution during solidification, we coupled grain-scale cellular automata (CA) [60–62] with the multiphysics deposition model discussed in Section 3.1 through the temperature field and phase distribution (void, liquid, solid). The CA model accounts for epitaxial nucleation and orientation-dependent growth of prior  $\beta$  grains. For the sake of simplicity, heterogeneous nucleation ahead of the solidification front during laser processing and solid-state transformation were omitted from the considerations. To clarify on the former assumption, heterogeneous nucleation ahead of the solidification front during LPBF of Ti6Al4V is often disregarded in simulations [63–66]. This assumption is based on the inherent steep thermal gradients in LPBF, which inhibit such nucleation. In castings, equiaxed grains can form from the detachment of secondary dendrite arms within a mushy zone. However, in LPBF conditions, this mushy zone is extremely narrow due to steep thermal gradients, making the detachment mechanism unlikely. Moreover, in Ti6Al4V alloy, the high partition coefficients of the primary alloying elements (close to one [67,68]) reduce the degree of constitutional undercooling ahead of the solidification front, resulting in a low likelihood of grain nucleation.

As the CA algorithm has been detailed in our previous studies [60–62], in this section we will briefly overview only its basic principles. The CA model evolves in time, tracking the states of individual CA cells (voxels) and the local environment of cells (neighborhood, temperature field, phase distribution field). Each voxel can exist in one of four states: liquid, undercooled liquid where  $T < T_{\rm L}$ , the interface, or solid. Here  $T_{\rm L}$  (K) is the liquidus temperature. The transition between these states follows specific rules set out in our earlier publications (see Table 5 in [60]). The first-order Moore neighborhood is considered.

First, the microstructure of the initial setup is generated via nucleation and growth of grains. The seeds are randomly distributed in the domain, with their number determined based on the average grain size reported in the literature. The method we previously introduced was employed to determine the crystallographic orientations of the crystals, aiming to produce a material without texture. Each growing CA cell is associated with a so-called grain envelope shaped as a regular octahedron in 3D. The octahedron connects the preferred growth directions of a crystal, (100) in cubic crystals. The expansion of this octahedron, which happens by the growth of its diagonals aligned with the crystal's preferred growth directions, is governed through temporal integration of the growth kinetics. The growth kinetics relates the grain growth velocity  $\nu$  (m.s<sup>-1</sup>) with the undercooling  $\Delta T$  (K) as  $\nu = A\Delta T^2$ . Here A represents the material dependant constant calculated to fit the predictions of lower-scale models and in this work is set to  $5.85 \times 10^{-6}$  (m. s<sup>-1</sup>.K<sup>-2</sup>) [62]. To address the challenge of artificial anisotropy introduced by the voxel mesh - a common issue in CA modeling - we implemented a modified decentred octahedron algorithm [69]. The centre of the octahedron in the  $i^{th}$  CA voxel is defined at the moment when the  $i^{\mathrm{th}}$  voxel gets nucleated or captured by a growing crystal, at the location where it was captured. As the grain expands, the octahedron reaches out to neighboring 'undercooled liquid' voxels, incorporating them into the growing crystal and transferring the crystallographic orientation and grain index (unique integer value for each grain). This process continues until all neighboring CA cells are classified as either 'solid' or 'growing', at which point the grain envelope solidifies

completely, no longer participating in the solidification front. After the microstructure of the initial setup was generated, we subjected it to virtual laser irradiation using the multiphysics deposition model. The CA simulations coupled with the thermal field resulting from the multiphysics CFD model were performed on Gadi, the peak supercomputer of the National Computational Infrastructure (NCI, Australia).

#### 4. Model validation

In this section, the validation of the developed multiphysics model is presented. Several single tracks were manufactured using the LPBF machine detailed in Section 2. The single-track specimens were manufactured using two laser modes, RSBP and GBP at two different powers 250 W and 500 W power at 1000 mm.s<sup>-1</sup> scanning speed. In order to have a closer agreement between the multiphysics model and the experiments in terms of process conditions, the parameters in Eq. (8) are selected in such a way that they resemble the actual measured laser heat flux. This would then enable us to systematically change the beam indices in the subsequent sections for detailed investigations. Fig. 4(a) and (c) show the 2D view as well as the distribution of the heat flux for RSBP in the simulation. Fig. 4(b) and (d) show the experimentally-measured profiles of the RSBP using a profilometer.

According to Fig. 4, there are a number of minor discrepancies between the simulated and the experimentally-measured beam profiles and these could be ascribed to instantaneous laser power fluctuations as well as imperfect laser heat flux distribution that in reality could deviate from the idealized distribution described with the analytical function in Eq. (8). The predicted three-dimensional temperature contours along with the spatial laser heat flux distribution over the melt pool using RSBP shown in Fig. 4 are displayed in Fig. 5. According to the blowup images, it is noted that an RSBP leads to a distinct depression zone composed of a core depression and an annular depression, in contrast to the single depression forming in regular LPBF processes with singlemode GBPs [70-72]. Locating the positions of these two depression points and matching them with the laser distribution reveals that the depression zones are directly caused by the local peak values of the core (central) and the annular (ring) parts of the laser heat flux distribution, based on Fig. 5. The deposition-scale simulations were run on 64-core workstations with AMD Ryzen Threadripper PRO 5995WX @4.5 GHz system with 256 GB RAM and it took about 7 hours and 40 minutes on average to run the single track validation case.

The detailed predicted and observed melt tracks' dimensions for four different cases are shown in Fig. 6.

The comparison between the predicted and observed track cross-sections for four single tracks is shown in Fig. 6. For the RSBP, at both laser powers of 250 W and 500 W, the melt pool is at conduction mode without any keyhole depression zone formation [73,74]. Furthermore, it is noticed that due to the collective impact of the two depression zones caused by the core and ring part of RSBP, a significant portion of the melted material is redeposited to the center of the track while leaving two line-indentations along the path of the laser coinciding with the footprints of the ring part of the laser. This would eventually result in the track morphology shown in Fig. 6 for RSBP 500 W and the underlying physics can be explained by the physics of hump formation in LPBF using the GBP [75].

The simulated melt pool width for RSBP 500 W is found to be 348  $\mu m$  which is only 1.46 % larger than the experimental melt pool width of 343  $\mu m$ . The predicted melt pool depth is found to be slightly larger than the experimental value and this led to an error of 8.77 %. The larger deviation in terms of predicted melt pool depth could arise from the fact that in the simulations, as we are using analytical expressions, the laser heat flux is marginally larger than that in reality, and this was visible from Fig. 4(a) – (d). For the GBP with 500 W, the predicted melt pool width and depth are 234  $\mu m$  and 180  $\mu m$ , respectively – leading to a width-to-depth ratio of 1.3. The width-to-depth ratio for the melt pool with RSBP is found to be 5.61 which is significantly larger than the ratio

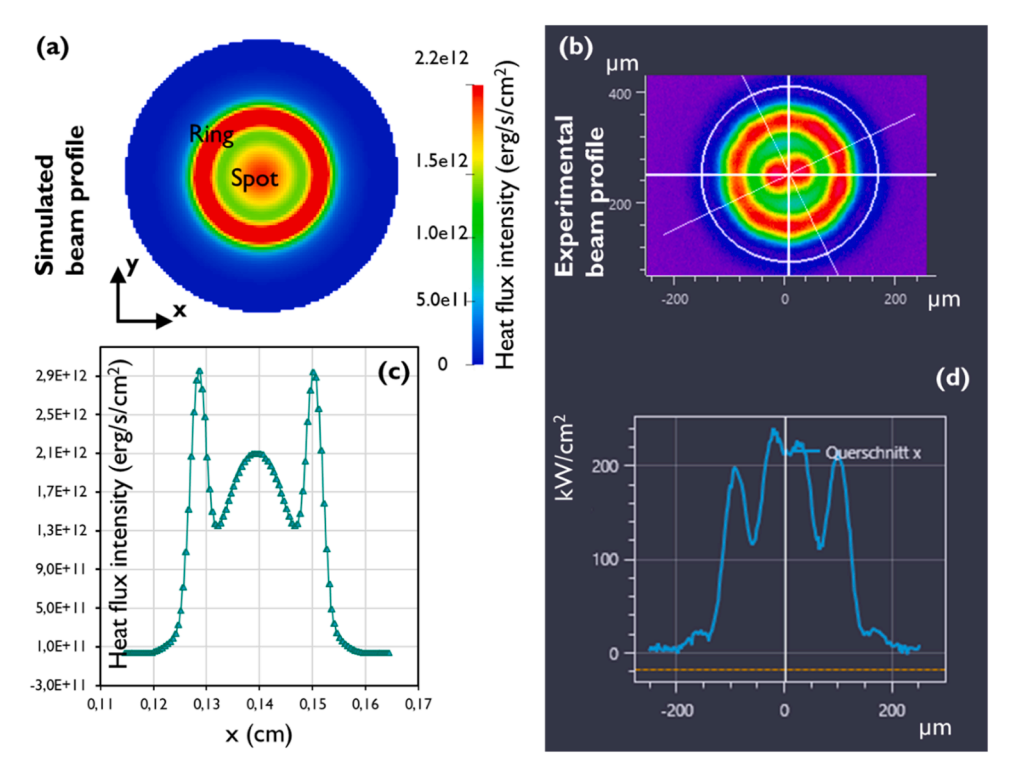


Fig. 4. Details of the RSBP for validation. (a) 2D view of the implemented RSBP in the simulation, (b) experimental laser beam profile contour and (c) and (d) show the modelled and experimentally-measured laser heat flux for RSBP, respectively. It is worth noting that the comparison is made for a static laser at 200 W laser power. The German word Querschnitt stands for cross-section.

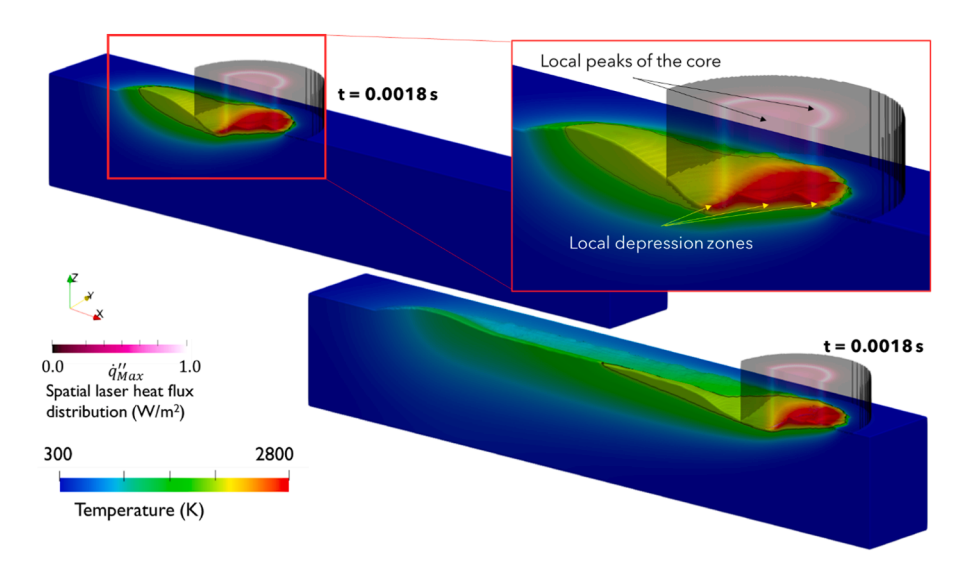


Fig. 5. 3D temperature contour and laser heat flux distribution using RSBP 500 W at two different times of 0.0004 and 0.0018 seconds. The black isoline shows the border of the melt pool.

for GBP which is typically in the range of unity or below that depending on the melt pool regime [76,77]. Therefore, it is believed that RSBP could potentially boost the build rate with fewer tracks, but this comes with the downside of having improper cross-layer bounding or sintering that could plausibly lead to internal porosities due to lack of sintering. In conclusion, the results presented in this section show a very good agreement between the predicted and experimental single-track profiles and the subtle error percentage of less than 9 % supports the validation of the multiphysics simulation of LPBF with a RSBP laser.

#### 5. Results and discussions

This section is divided into two subsections; in the first subsection, we delve into the impact of different beam modes on the predicted heat and fluid flow and microstructural conditions during LPBF of a titanium alloy using four different modes ranging from GBP to RBP. The next subsection is focused on the role of RBP in LPBF and here, numerical and *in-situ* online experimental data are presented, discussed and compared.

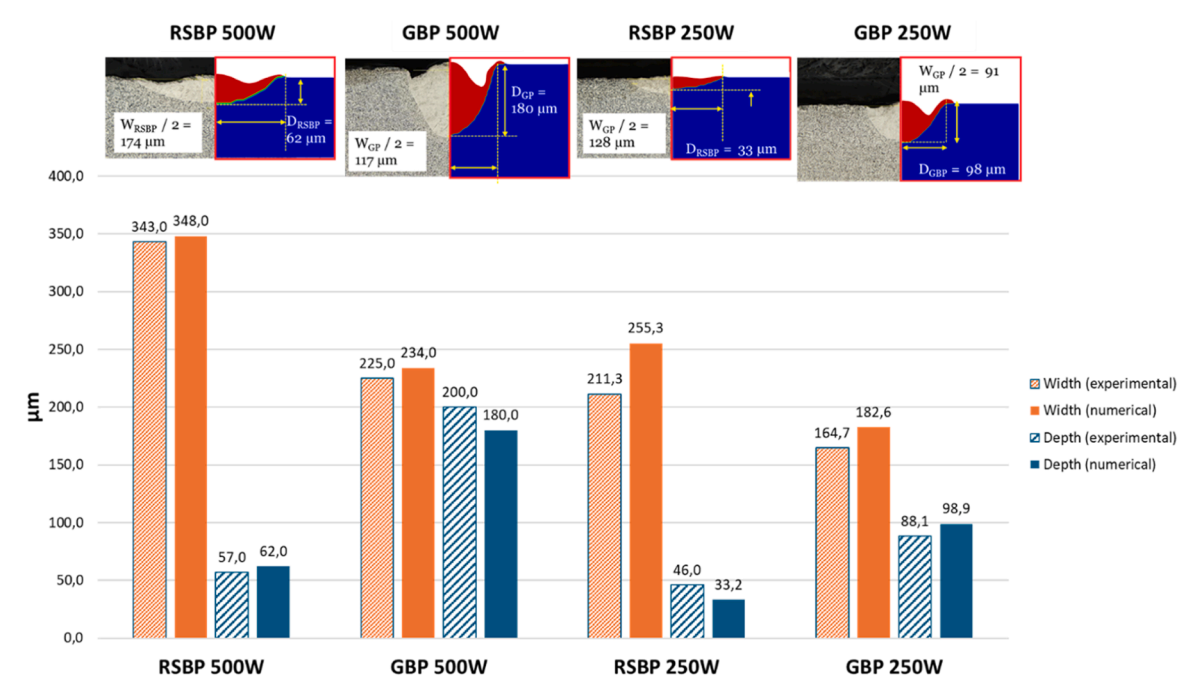


Fig. 6. Comparison between the predicted and experimentally observed track dimensions for four single track experiments; RSBP with 250 W and 500 W and GBP with 250 W and 500 W.

#### 5.1. The impact of beam modes

The beam shapes range from a GBP with a core-to-ring ratio of 6:0 to an RBP with a core-to-ring ratio of 0:6. Two intermediate core-to-ring ratios of 4:2 and 2:4 with an RSBP are considered in between the GBP and RBP. Table 1 gives an overview of the implemented process parameters.

Fig. 7 shows the dimensionless laser heat flux distribution for the four beam shapes listed in Table 1.

According to Fig. 7 and Table 1, all of the laser power is concentrated in the center or core of the GBP. Conversely,  $100\,\%$  of the laser power is distributed over the ring in the RBP and for RSBP1 and RSBP2,  $66.6\,\%$  and  $33.3\,\%$  of the laser power are concentrated at the center of the laser beam. Fig. 8 shows a three-dimensional view of the calculated temperature contours along with the implemented laser heat flux distribution for the four cases with low laser power introduced in Table 1.

Based on Fig. 8, it is noted that lowering the core/ring ratio leads to shallower and at the same time wider melt pools. Even though the laser

**Table 1**Process details for beam mode parametric study. Note that L stands for low and H stands for high.

P (W)	v (mm. s <sup>-1</sup> )	R (µm)	a (µm)	Tag	Description	Core: ring
140	700	100	42	L-GBP	Gaussian beam profile – low power	6:0
				L- RSBP1	Ring spot beam profile – low power	4:2
				L- RSBP2		2:4
				L-RBP	Ring beam profile – low power	0:6
250	700	100	42	H-GBP	Gaussian beam profile – high power	6:0
				H -RSBP1	Ring spot beam profile – high power	4:2
				H -RSBP2	- 01	2:4
				H -RBP	Ring beam profile – high power	0:6

power is identical in all cases, the melt pool depth is the largest in the GBP case. Details regarding the melt pool dimensions using the process parameters listed in Table 1, are given in Table 2.

According to Table 2, the width/depth ratio increases from 0.8 (typically observed for LPBF with the GBP [77-79]) to 3.3 when using the GBP and RBP, respectively. This is as expected because the entire laser power in the GBP is concentrated within a circle with a radius of 42 µm, as compared to the other extreme case, the RBP, where the power is distributed over a ring with a radius of 100 µm. Based on Table 2, it is also noted that the length/depth ratio increases while raising the ring contribution. This ratio is 3.94 for L-GBP and is less than 40 % of the one for RBP, which is 10.93. This is because for the L-GBP, the recoil pressure is quite high, and this leads to the movement of the entire melt pool downwards. For the melt pool using RSBP beams, as the irradiated zone is larger due to the existence of the ring part, the melt pool will be wider. Thus the Marangoni number will be larger as well, since  $Ma \equiv (|\gamma| \bullet (\Delta T)$  $L_{CH}$ )/( $\alpha \bullet \mu$ ). Also, according to [53], ordinary alloys and metals with negative  $\gamma$  will induce radially outward flows that tend to widen the melt pool as the Marangoni effect advects hot liquid metal to the rims of the melt region. Fig. 9 shows a closeup of the melt pool temperature under L-GBP and L-RBP, respectively.

The localized heating caused by using the GBP leads to high surface temperatures at the center of the melt pool in contrast to the relatively colder surface temperature at the center of the melt pool when using the RBP. This is a consequence of the energy being far less localized or concentrated in the RBP case.

Fig. 10 shows the temperature contours for the last four beam modes described in Table 1 at the high laser power of 250 W. Details of the melt pool dimensions are listed in Table 3.

Similarly to the first four cases with 140 W laser power, the melt pool depth is seen to be decreasing with an increase in the ratio of the ring profile's contribution. It is observed in Fig. 10 (b) that the deepest point in the melt pool forming under the RBP occurs over the melt pool rims where the laser heat flux is highest – unlike melt pools forming under the influence of the GBP. Whereas, for the rest of the cases, which are a pure GBP or a combination of a GBP and a RBP, the deepest point of the melt pool coincides with the center of the laser beam, see Fig. 10 (d), (f) and (h).

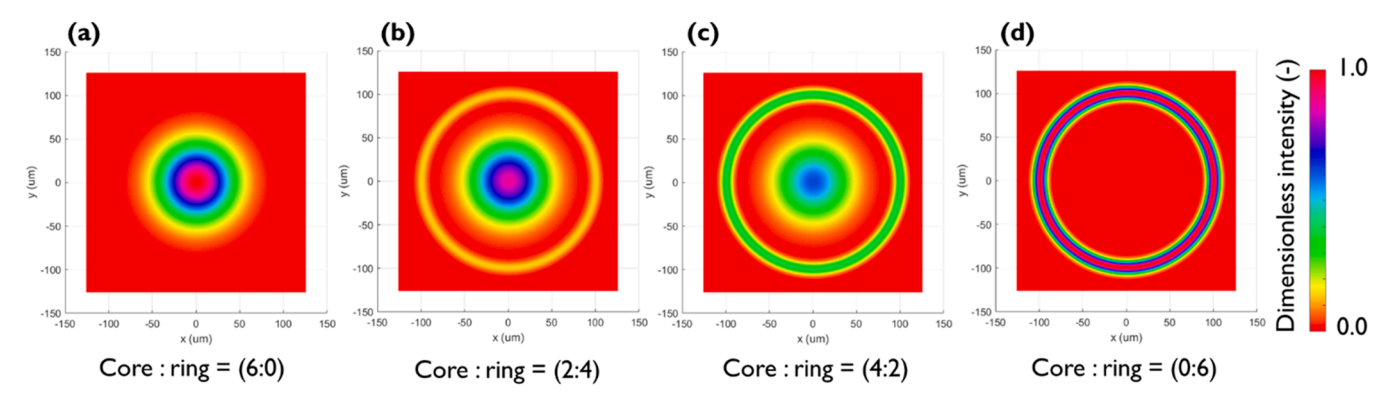


Fig. 7. Dimensionless laser heat flux distribution for (a) GBP - 6:0, (b) RSBP1 - 4:2, (c) RSBP2 - 2:4 and (d) RBP - 0:6.

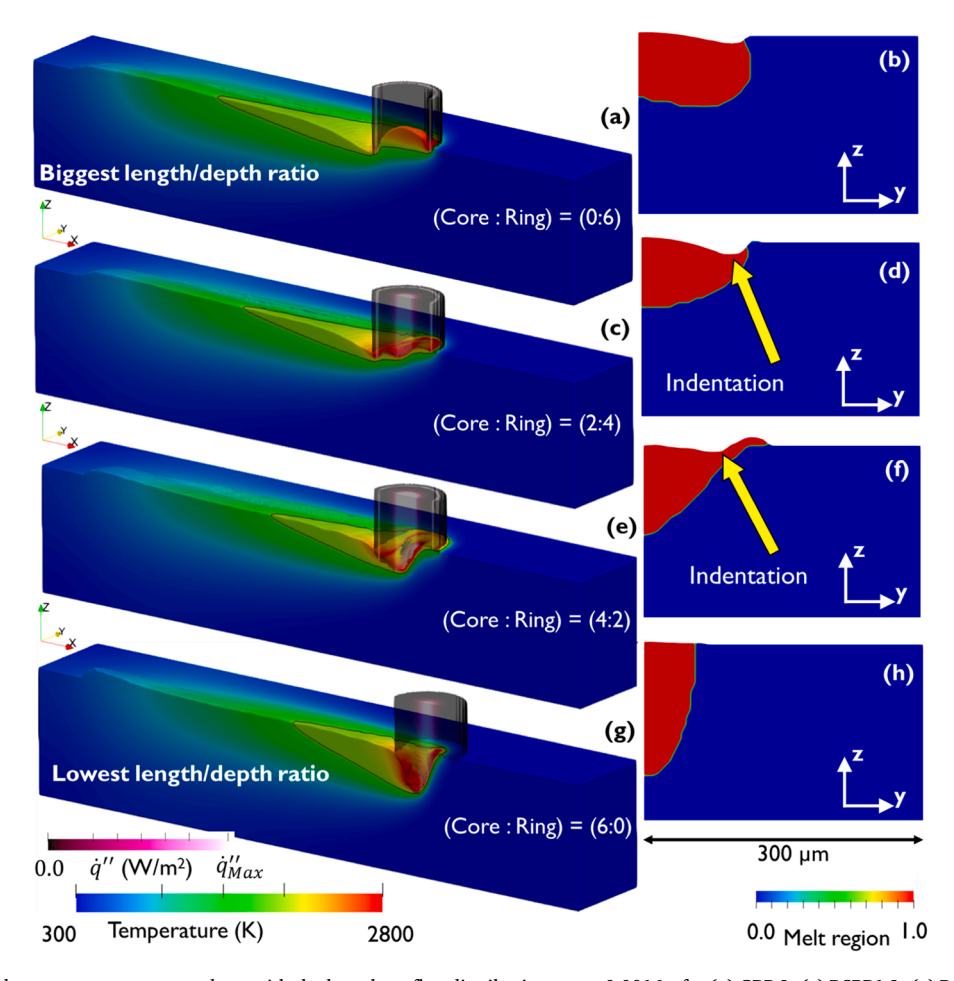


Fig. 8. Three-dimensional temperature contours along with the laser heat flux distribution at t = 0.0016 s for (a) GBP-L, (c) RSBP1-L, (e) RSBP2-L and (g) RBP-L. (b), (d), (f) and (h) show the corresponding cross-sections of the melt region at the center of the scan track for these four beam profiles.

**Table 2** Calculated melt pool dimensions for 140 W and 700 mm.s $^{-1}$  scanning speed.

Beam index	Width / 2 (um)	Length (um)	Depth (um)	Width/ depth (-)	Length/ depth (-)
L-GBP	56.2	555.0	140.9	0.8	3.94
L-RSBP1	131.2	635.5	96.6	2.7	6.58
L-RSBP2	115.2	698.2	69.3	3.3	10.08
L-RBP	122.3	806.2	73.8	3.3	10.93

According to Table 3, the width/depth ratio of the melt pool with the GBP laser is 0.54, which is close to the keyhole melt pool morphology [76] while the width/depth ratio for the rest of the cases is larger than one.

As noted in Fig. 10 (a), the melt pool becomes highly unstable and enters a splashy regime for the RBP at 250 W, whereas the melt pool under the same beam profile but at a lower laser power of 140 W is relatively stable and is in the conduction regime, as previously observed in Fig. 8(a). To have a clearer insight into the melt pool's regime transition due to the laser power increase under the L-RBP, two snapshots of the temperature contour at  $t=10^{-4}$  and  $6\times10^{-4}$  seconds are shown in Fig. 11 (a) and (b).

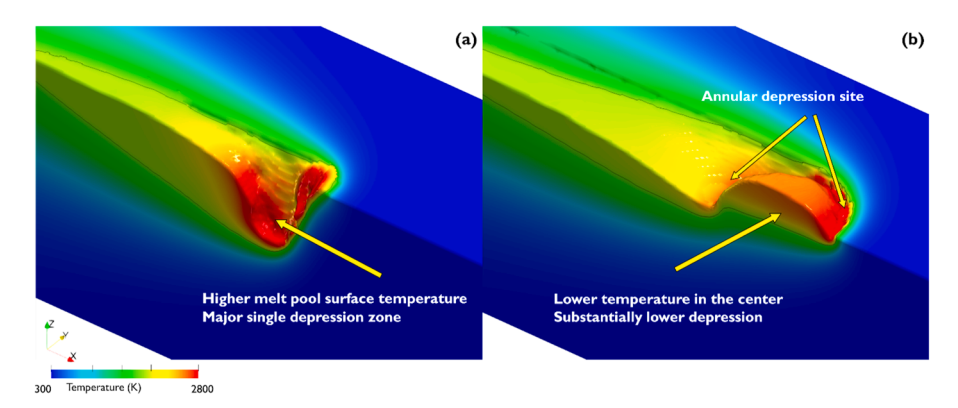
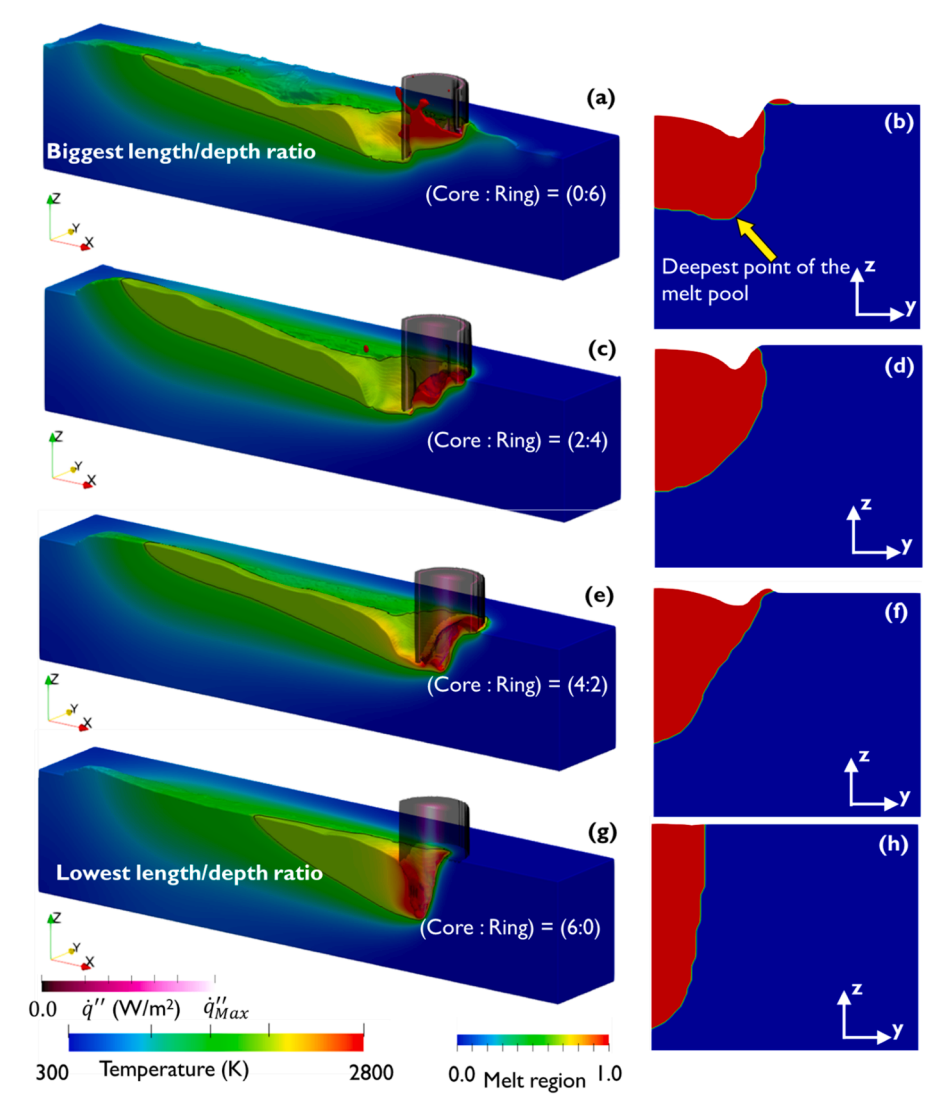


Fig. 9. A zoomed view of the temperature contour and depression zones for (a) L-GBP and (b) L-RBP at  $t=0.0015 \ s.$ 



**Fig. 10.** Three-dimensional temperature contours of temperature along with the laser heat flux distribution at t = 0.0016 s for (a) H-GBP, (c) H-RSBP1, (e) H-RSBP2 and (g) H-RBP. (b), (d), (f) and (h) show the corresponding cross-sections of the melt region at the center of the scan track for these four beam profiles.

It is evident from Fig. 11 (a) that the melt pool starts growing from a ring-shaped profile at the very start of the scanning process and that the temperature is high enough such that an annular depression zone is instantly formed even at this very early stage of the process. The melt pool remains stable until the end of the process and conserves its surface morphology as it reaches the quasi-steady state condition - a

characteristic of stable melt pools in LPBF [80]. The active annular depression zone leads to a bulge in the center of the front part of the melt pool as the core part of the laser beam is absent under the RBP. The bulge formation is, therefore, only specific to RBPs, as for other beam shapes with GBP elements, the contribution of the core part of the laser beam balances the bulge and evens it out as the central recoil pressure

**Table 3**Calculated melt pool dimensions for 250 W and 700 mm.s<sup>-1</sup> scanning speed.

Beam index	Width / 2 (µm)	Length (µm)	Depth (um)	Width/ depth (-)	Length/ depth (-)
H-GBP	60.63	780.84	225.72	0.54	3.46
H-RSBP1	128.61	1203.74	171.92	1.50	7.00
H-RSBP2	125.20	1313.88	162.20	1.54	8.10
H-RBP	133.33	1238.99	129.40	2.06	9.58

becomes more substantial.

Looking deeper into this, according to Fig. 11 (d), the annular depression zone causes the relocation of the liquid metal to the center of the track as the material is incompressible. Furthermore, one can also see that, close to the bulge location, the Marangoni-driven lines are pointing to the center of the melt pool - opposite to what is typically observed in LPBF or melting-based processes where thermo-capillarity induces an outward flow of liquid metal [53,81] and this originates from lower center temperatures for melt pools when using the RBP. Nevertheless, on the melt pool scale level, the Marangoni-induced velocity vector field shown in Fig. 11 (c) causes a typical flow direction towards the tail of the melt pool.

The predicted temperature contour for the higher laser power of 250 W applying the RBP is shown in Fig. 12 (a) and (b) at the two instants in time of  $10^{-4}$  and  $6\times10^{-4}$  seconds, respectively. The melt pool formed at  $10^{-4}$  seconds has a more noticeable depression zone as compared to the one at the same instant in time with 140 W laser power, see Fig. 11 (a) and (c). This, as shown in Fig. 12 (a), would naturally result in a larger liquid metal displacement as the recoil pressure is more pronounced. The more significant liquid metal displacement, even at the very early stage of the scanning process, leads to an apparent elongation of the bulge forming in the center of the laser beam, see Fig. 12 (a). As the process continues, the central bulge transforms into a jet-like flow that is directed upwards and opposite to the direction of the recoil pressure. The formation of this central jet is even more clearly displayed in Fig. 12 (c) and (d) and the height of the jet reaches about 150  $\mu$ m from

the depression zone.

Fig. 13 shows a side view of the sequence of the melt pool transformation at 250 W laser power taken at four different times. One can see that the melt pool instability can be explained by the four distinct stages: (I) early-stage breakup of the liquid jet, (II) total breakup of the jet, (III) material remelting and redistribution, and (IV) reformation of the liquid metal jet. According to Fig. 13 (a), the central liquid metal jet grows up to a certain level during which the surface tension of the liquid metal is not able to keep the jet together any longer and therefore, it collapses and subsequently breaks up and forms liquid spatters, similar to the form of spatter in [81,82].

The breakup of the central liquid metal jet shown in Fig. 13 (a) is caused by the collective impact of two phenomena: first, the lowered surface tension at the center due to laser heating and this automatically reduces the capability of the material to contain the liquid metal jet and second, the high speed of the central jet, which makes it even more difficult for the already-lowered surface tension to keep the bulge together. As a consequence, the liquid jet breaks up into smaller droplets with such high velocities that some even get deposited on the work piece again, hence increasing the risk of unwanted and higher levels of surface roughness compared to when employing a GBP, as reported by [38]. After the collapse of the liquid metal jet, the laser starts melting the material again and this in turn increases the volume of the liquid phase, see Fig. 13 (c). In a matter of 0.2 ms, it is observed that the liquid metal jet re-establishes itself and reaches a height of ca. 100 µm, see Fig. 13 (d). The four-stage loop repeats during the course of the process and this leads to significant spatter formation and instability of the melt pool.

In conclusion, one can say that the RBP could potentially increase productivity as it covers wider regions, compared to the more concentrated GBP. Thus, the use of RBPs requires lower numbers of hatches, but as a downside, the melt pool that forms under the use of RBPs becomes highly unstable at higher laser powers due to the formation of the mentioned liquid metal jet at the center of the melt pool. This means that the RBP has a fairly limited process window, since such instabilities might arise when the power is increased. A solution to this drawback of RBPs is using lower laser power - hence keeping the melt pool regime in

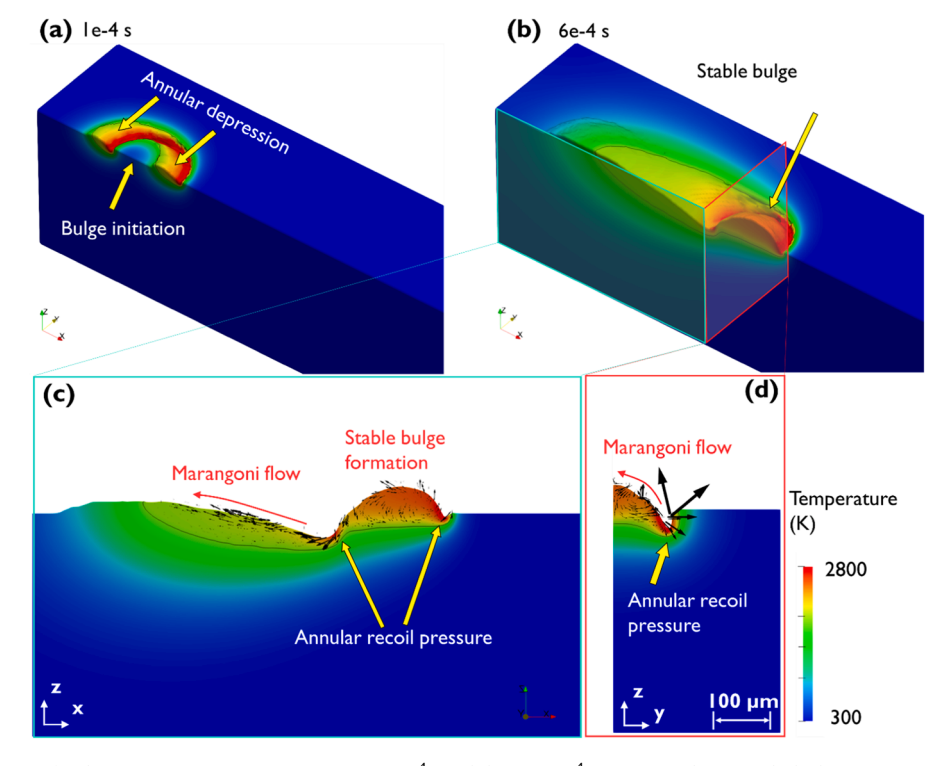


Fig. 11. Temperature contours for the RBP at 140 W (L-RBP) at; (a)  $t = 10^{-4}$  s and (b)  $6 \times 10^{-4}$  s, respectively. (c) and (d) show cross-sectional views of the melt pool at  $t = 6 \times 10^{-4}$  s from (c) side view in the x-z plane and (d) front view in the y-z plane. The y-z plane is precisely at the location of the center of the RBP laser.

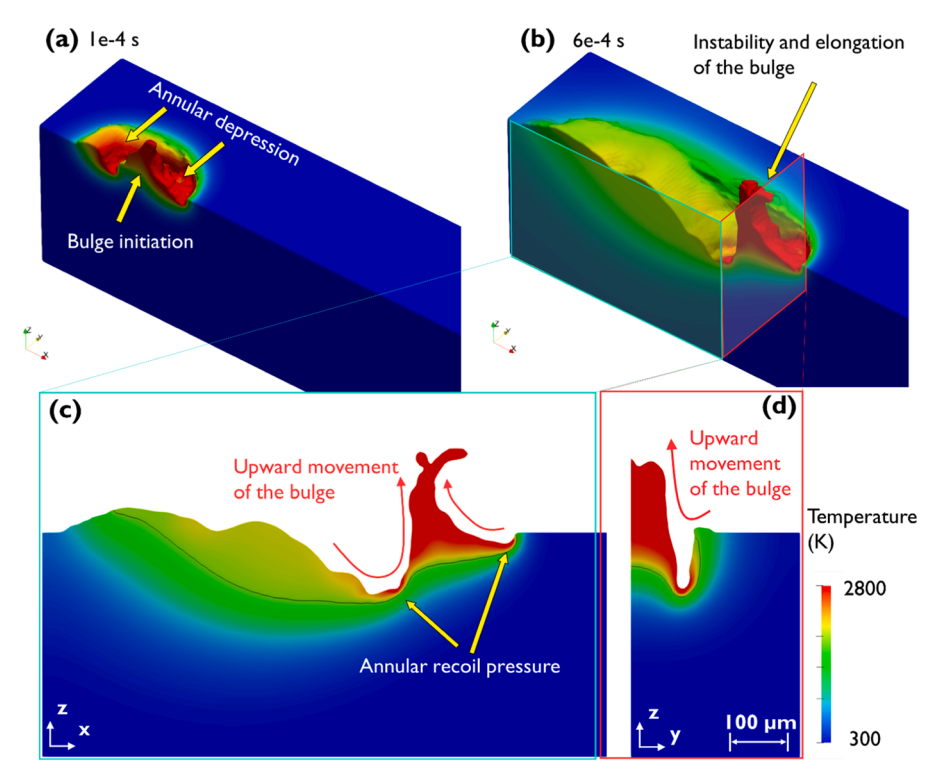


Fig. 12. Temperature contours for the RBP at 250 W (H-RBP) at; (a)  $t = 10^{-4}$  and (b)  $6 \times 10^{-4}$  s, respectively. (c) and (d) show cross-sectional views of the melt pool at  $t = 6 \times 10^{-4}$  s from (c) side view in the x-z plane and (d) front view in the y-z plane. The y-z plane is precisely at the location of the center of the RBP laser.

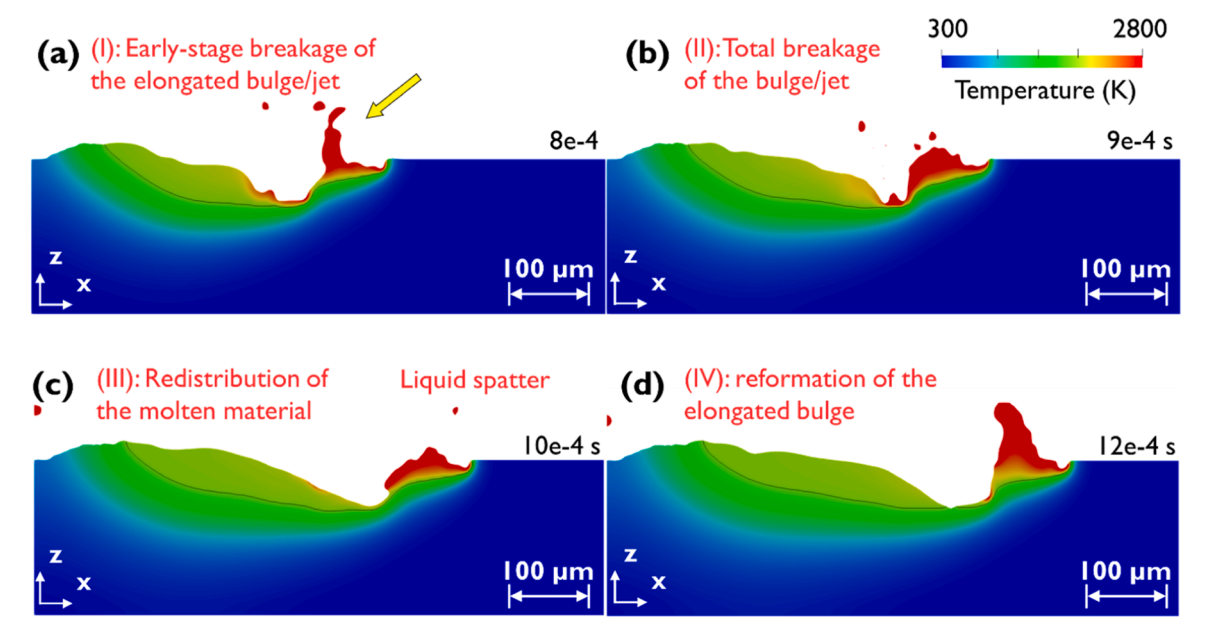


Fig. 13. Side view of the predicted melt pool temperature employing RBP at 250 W laser power at: (a)  $8 \times 10^{-4}$  s, (b)  $9 \times 10^{-4}$  s, (c)  $10 \times 10^{-4}$  s and (d)  $12 \times 10^{-4}$  s.

the conduction mode [76]. However, the shortcoming of this strategy is insufficient melt pool depth which can potentially cause lack of bonding between two neighboring powder layers.

After obtaining the temperature field at the deposition-scale, we did the CA calculations at the micro-scale where we applied an initial grain size of 2  $\mu m$ . The computational domains considered for the H-GBP and H-RBP (with 250 W power and 700 mm.s $^{-1}$  scanning speed) modes were of size  $179\times2029\times273~\mu m^3$  and  $296\times2146\times179~\mu m^3$  (y  $\times$  x  $\times$  z), respectively, with the CA cell size of 1  $\mu m$ . These simulations took 52 and 79 min, respectively, on  $2\times52$  core Sapphire Rapids of NCI Gadi.

Note that the comparison in this subsection is more of a qualitative nature and focuses on identifying trends.

Fig. 14 demonstrates the central y-z cross-sections of the model samples depicting the grain structures observed in single tracks using H-GBP (a) and ring H-RBP beams (b). The microstructure of a single track, particularly the shape and orientation of grains, is shaped by the thermal conditions within the melt pool. During solidification, the 'ease' with which a grain grows depends on the alignment of its preferred growth directions with the steepest thermal gradient. For cubic alloys, the preferred growth direction is typically <100>, which has been shown to

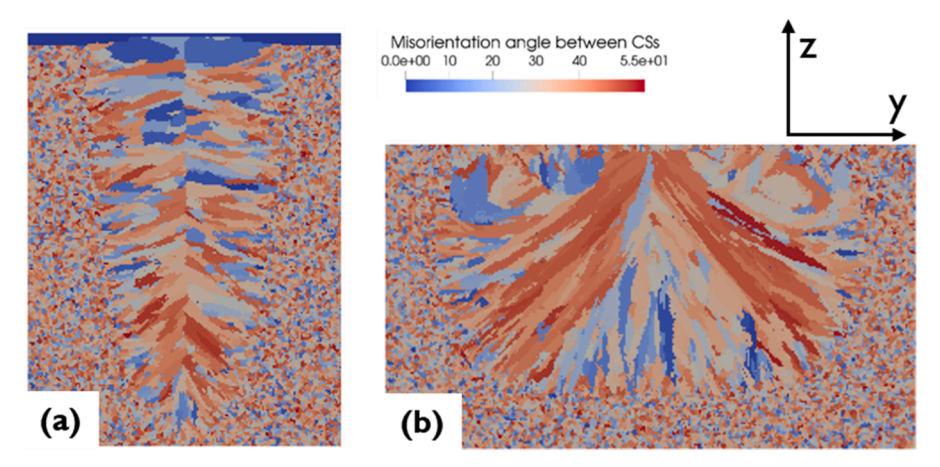


Fig. 14. Model-predicted grain structures in the central y-z cross-sections for (a) H-GBP and (b) H-RBP. The initial average grain size of the base plate is 2  $\mu$ m. The colour depicts the misorientation angle between the z-axis of the sample coordinate system and the closest <100> direction of the crystal coordinate system; CS in the scale title stands for the coordinate system.

yield the highest growth rates for body-centered cubic and face-centered cubic grains [83]. According to the solidification theory, grains with growth directions that align well with the thermal gradient grow preferentially over those misaligned with the heat flow. The result is competitive growth. In both cases studied, the grain growth orientations are approximately perpendicular to the liquidus isotherm at each local point.

In both cases, the grain growth orientations are approximately perpendicular to the fusion line. The H-GBP mode mainly produces long columnar grains along with a smaller number of short-range columnar grains and some quasi-equiaxed grains (Fig. 14 a). These columnar grains grow from the boundary of the melt pool to its centerline. They grow slightly upwards at an angle, aligning with the maximum thermal gradient. This gradient depends on the melt pool shape. The H-GBP mode produces a deep and narrow melt pool, with its centerline (Fig. 14 a) solidifying last. This solidification behavior causes grains to converge on one another along this centerline. Close to the root of the single track, where the melt pool becomes teardrop-shaped, the angle between the longest direction of a columnar grain and the melt pool centerline is larger than in the upper part of the melt pool, where it becomes  $\sim 90^{\circ}$ . This behaviour is characteristic of the deep, cup-shaped melt pools [84, 85]. Close to the root, the misorientation between the z-axis of the sample coordinate system and the closest <100> direction of the crystal coordinate system is predominantly larger than 40°, forming a region characterised by the prevalent crystallographic orientation of grains. The latter is well observed in the x-z cross-section parallel to the laser motion (Fig. 15 a). The fact that grains converge at the centerline of a

melt pool results in their appearance as equiaxed grains in the central x-z cross-section.

In the H-RBP mode, the microstructure does not follow a characteristic two-fold shape observed in the y-z cross-section (Fig. 10 b), opposite to the results reported in [86]. The reason for this is the large liquid metal displacement towards the central part of the melt pool due to more pronounced recoil pressure (Fig. 12 c). Primarily, the H-RBP mode results in the formation of long columnar grains, accompanied by some short-range columnar grains and a few quasi-equiaxed grains (Fig. 14 b). The bottom of the melt pool near the root region is planar, which results in columnar grains growing upwards from the melt pool boundary at its center and approximately parallel to the z direction (Fig. 14 b; Fig. 15 b). Growing upwards, these grains demonstrate columnar appearance in the central x-z cross-section, opposite to the equiaxed microstructure pattern observed in the H-GBP mode (Fig. 15). These grains are characterized by the less than 20° misorientation angle between the sample and crystal coordinate systems, forming a different predominant crystallographic orientation than in the GBP mode (Fig. 15). On the lateral sides of the melt pool, columnar grains of  $\sim 40^{\circ}$ misorientation angle are observed, which grow at the same angle towards the top central point of the melt pool (Fig. 14 b). In the top view (x-y cross section), the morphology of these grains will appear as equiaxed, which agrees with [86].

#### 5.2. In-situ comparison with X-ray monitoring data

In this subsection, the results from the numerical model are

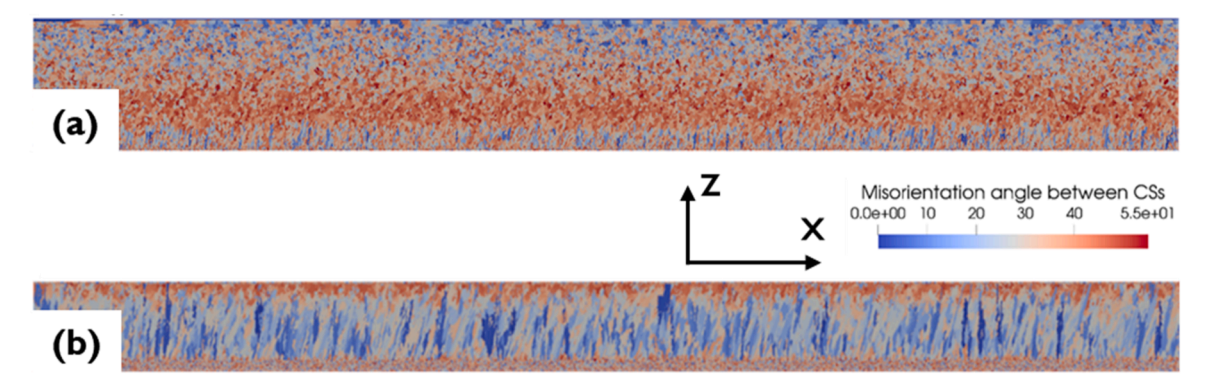


Fig. 15. Model-predicted grain structures in the central x-z cross-sections for (a) H-GBP and (b) H-RBP. The initial average grain size of the base plate is 2  $\mu$ m. The colour depicts the misorientation angle between the z-axis of the sample coordinate system and the closest <100> direction of the crystal coordinate system; CS in the scale title stands for the coordinate system.

compared with the data and images captured via X-ray *in-situ* monitoring setup described in Section 2.2. It must be emphasized that the comparison in this subsection is more of a qualitative nature than a detailed 1:1 comparison. Therefore, the process parameters are slightly changed to resemble the process conditions under which the single-track specimens for the *in-situ* X-ray CT imaging were manufactured. As the *in-situ* experiments are only done on the annular beam shape mode, we focus on the RBP models discussed in 3.1. In this respect, the scanning speed of the L- and H-RBP and models were modified to 500 mm.s<sup>-1</sup> to match the experimental conditions used in the *in-situ* imaging tests.

Fig. 16 compares the simulated and experimental melt pool cross-section from a side-view parallel to the scanning direction. According to Fig. 16 (a), the depression zone is formed right beneath the location where the laser heat flux is at its maximum for the RBP. This, as mentioned earlier, causes a bulge to form right beneath the laser beam. According to the numerical and experimental results shown in Fig. 16, the melt pool regime is stable without any signs of temporal changes in the shape and morphology – confirming reaching a quasi-steady state condition

Fig. 16 (c) and (d) show *in-situ* images of the melt pool profiles which are quite similar to the ones predicted by the multiphysics simulation shown in Fig. 16 (a) and (b). The depression zones' morphology noticed in the experimental images in Fig. 16 (c) and (d) agree quite well with the predicted depression zone in the model and the morphology of the depression zone, affirms the impact of the annular-like depression zone as noticed in the simulated results shown earlier.

A similar comparison is made in Fig. 17 (a) and (e), a more noticeable bulge is formed right below the laser beam. As the recoil pressure at higher laser power is more pronounced, this leads to a more significant material re-distribution in the form of a vertically elongated bulge or metallic jet below the laser beam position, see Fig. 17 (a) and (e). The low surface tension caused by the elevated temperature is not able to contain the growing liquid metal jet and as outlined in Section 5.1, this brings about an early-stage breakup of the liquid metal jet, see Fig. 17 (b) and (f). One can clearly observe the generation of fast-moving hot spatters at liquid state in Fig. 17 (b) and (f). It is furthermore noted that the spatter particles are highly inclined to the back of the melt pool along the displayed directions in Fig. 17 (c) and (g). Moreover, as a follow-up step to the early-stage breakup of the liquid jet, the entire column collapses, leading to multiple hot spatter particles, see Fig. 17 (c)

and (g). Subsequently, one can see that after the collapse of the liquid metal jet, remelting brings more material to the center of the melt pool and this ultimately triggers the regeneration of the bulge and as mentioned in the previous subsection, these stages of the jet collapse and regeneration repeat during the course of the process. The reason behind the significant hump formation seen in Fig. 17 (h) could be due to a high recoil pressure due to rapid fluctuation in the laser power or the gas plume (affecting effective laser absorptivity), and such rapid fluctuations typically occur in LPBF [87,88].

#### 6. Conclusion

In this work, a combined numerical and experimental investigation was carried out to uncover the impact of BS in LPBF of Ti6Al4V. More specifically, a multiphysics numerical model at the deposition scale, capable of simulating laser beams with varying intensity profiles was implemented. The model is developed in the commercial FVM solver, Flow-3D. To validate the multiphysics model, detailed experiments were performed where an RSBP was used to print single-track Ti6Al4V specimens. Comparing model results and *ex-situ* experiments showed a deviation of less than 10 % in predicted and measured melt pool dimensions for four cases with different process parameters.

To further investigate the impact of spatial beam shaping, several parametric studies were subsequently carried out. Firstly, four different beam shapes were studied in which the laser beam profiles spanned from a GBP to an RSBP and an RBP. Here, the power distribution ratio between the central and annular parts of the GBP and RBP, being the two extreme cases, were 6:0 and 0:6, respectively. The numerical results suggest that the deepest melt pool forms under the GBP, as expected. In contrast, the RBP results in the largest width-to-depth ratio, as the laser heat flux is quite delocalized as compared to the more concentrated laser profile in GBP.

Next, the detailed melt pool behavior during the RBP was explored and it was found that a liquid metal bulge forms at the center of the melt pool due to material relocation. The primary mechanism behind this was identified to be the annular-shape recoil pressure zone, which pressed the liquid to the center. The Marangoni effect was identified as a secondary reason, which, in the case of the RBP, transports liquid metal from the hotter rims of the melt pool to the relatively colder center where the laser heat flux is absent. This is unlikely to happen when using the standard GBP as the central bulge of the melt pool is wholly

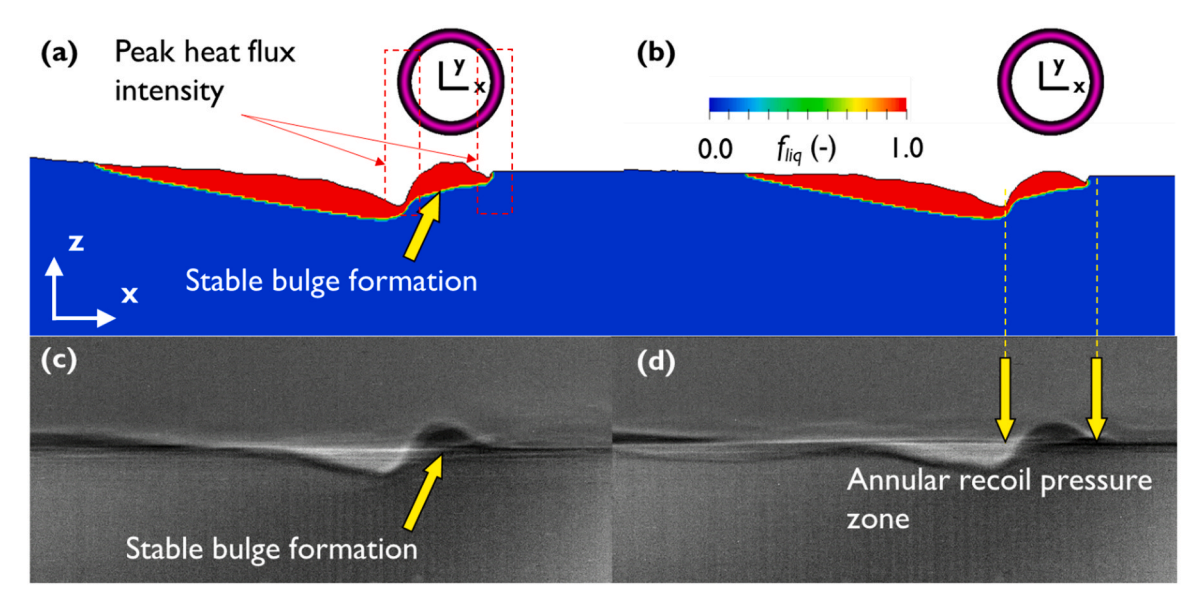


**Fig. 16.** Comparison between the simulated and *in-situ* experimental melt pool profile in the central plane parallel to the scanning direction for the low-power RBP case. (a) and (b) show the predicted melt pool's liquid fraction in the x-z plane at two different times when the melt pool has reached its quasi-steady state. (c) and (d) show *in-situ* images of the melt pool profile from a side view.

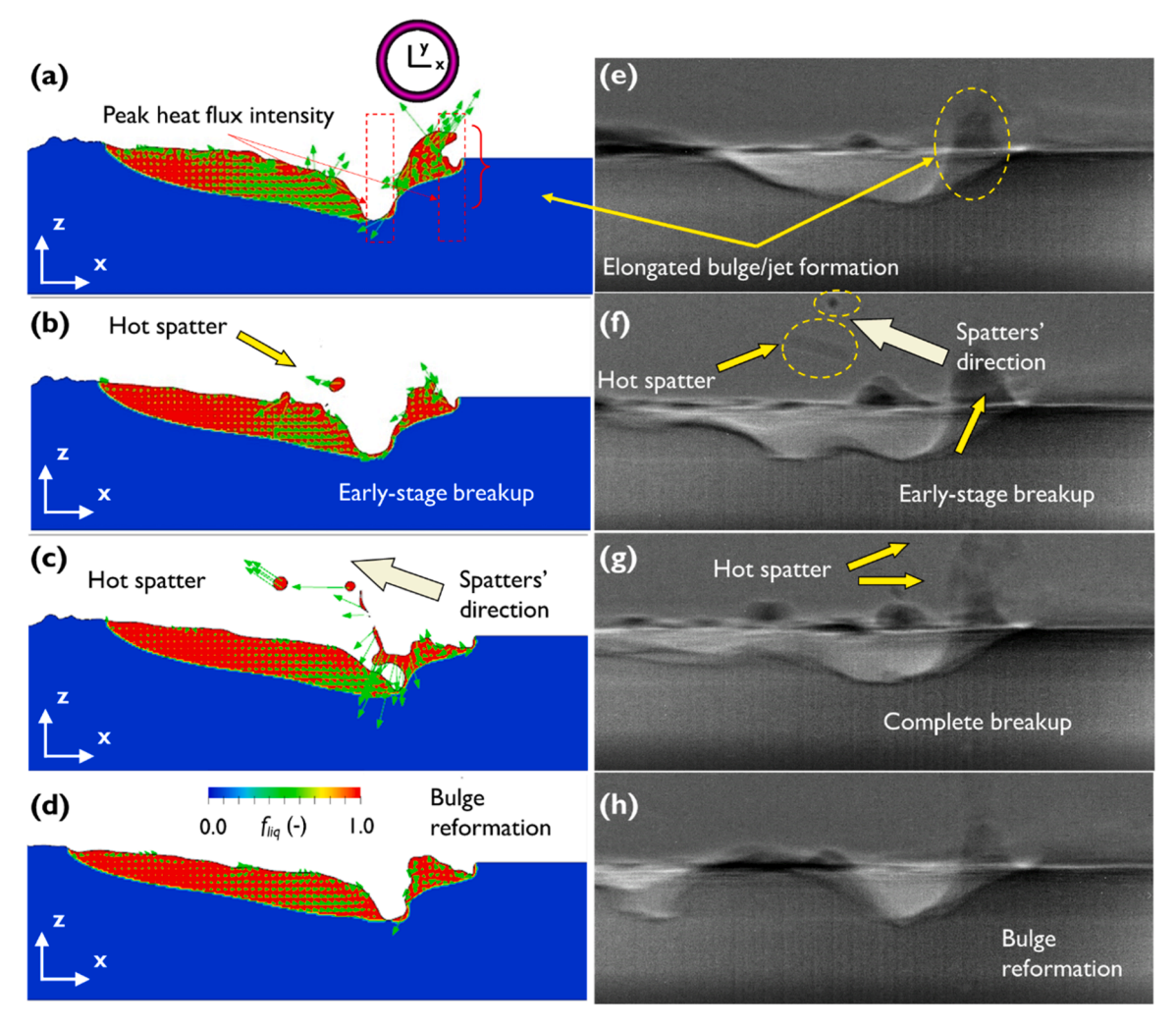


**Fig. 17.** Comparison between the simulated and *in-situ* experimental melt pool profile in the central plane parallel to the scanning direction for the high power case. (a) and (b) show the predicted melt pool's liquid fraction in the x-z plane at two different times. (c) and (d) show *in-situ* images of the melt pool profile from side view.

#### suppressed.

A further examination of the simulated results reveals that, at higher laser power, the central bulge undergoes a very unstable and undulating regime due to the significant recoil pressure along with the lowered surface tension. Here, the bulge transforms into a liquid metal jet pointing upwards which subsequently breaks up into liquid spatters splashing in various directions, however, mostly backwards opposite to the scanning direction.

To further validate the model, the simulated melt pool behavior was compared with *in-situ* X-ray images taken when using the RBP, and a good agreement was found. It was specifically noted that the melt pool undergoes a very unstable regime at high laser power, whereas at lower power, it is quite stable, with a bulge forming at the center.

Finally, CA simulations were carried out based on the model developed by the author group to predict the final grain morphology using the GBP and RBP. We found that during the former, the grains primarily grow to the centerline of the track, whereas during the latter, they tend to converge to a single point at the top of the melt pool.

In conclusion, it is evident that one can manipulate the melt pool dimensions to a large extent by tuning or modulating the spatial beam profile. As opposed to traditional process parameter variation consisting mostly of laser power and scanning speed variations, BS potentially entails more considerable flexibility, as confirmed via employing RBPs or RSBPs, obtaining width-to-depth ratios in the order of 5 and 6. Such substantial width-to-depth ratios are quite useful in terms of

productivity increase, as a lower number of hatches per layer would be needed. One potential downside, however, is the lower melt pool depth obtained by RSBPs or RBPs, which can be problematic when high layer thicknesses are targeted. Future research should address multi-track and multi-layer LPBF with RSBPs and RBPs and even temporally-modulated beam shaping to tailor the part's microstructure alongside the spatial modulation, as investigated here.

#### CRediT authorship contribution statement

Karen Schwarzkopf: Writing – review & editing, Visualization, Methodology, Investigation, Formal analysis. Aleksandr Zinoviev: Writing – review & editing, Writing – original draft, Methodology, Investigation. Olga Zinovieva: Writing – review & editing, Writing – original draft, Investigation, Formal analysis. Christoph Spurk: Writing – review & editing, Methodology. Mark Hummel: Writing – review & editing, Methodology. Alexander Olowinsky: Writing – review & editing, Methodology. Felix Beckmann: Writing – original draft, Methodology. Julian Moosmann: Writing – review & editing, Methodology. Michael Schmidt: Writing – review & editing, Supervision, Resources, Project administration, Methodology, Funding acquisition. Jesper H. Hattel: Writing – review & editing, Supervision, Resources, Project administration, Funding acquisition. Mohamad Bayat: Writing – original draft, Visualization, Validation, Software, Methodology, Investigation, Formal analysis, Conceptualization. Richard Rothfelder:

Writing – review & editing, Investigation, Conceptualization.

#### **Declaration of Competing Interest**

We, the author group, have no conflict of interest to declare.

#### Data availability

The data that has been used is confidential.

#### Acknowledgments

MB acknowledges receiving funding from the Danish-funded project microAM funded by Villum fonden (MicroAM-VIL54495). JHH received funding from the Horizon Europe CL4 project 101138289, GlobalAM. OZ and AZ acknowledge UNSW Resource Allocation Scheme at NCI [project mz70]. This work was also funded by the Deutsche Forschungsgemeinschaft (DFG, German Research Foundation) – 434946896. The authors acknowledge support by the Deutsche Forschungsgemeinschaft (DFG, German Research Foundation) for the collaborative research centre 814 "Additive Manufacturing" transfer project T08 (CRC814/T08 - 61375930). The authors gratefully acknowledge the funding of the Erlangen Graduate School in Advanced Optical Technologies (SAOT) by the Bavarian State Ministry for Science and Art.

#### References

- [1] C. de Formanoir, M. Hamidi Nasab, L. Schlenger, S. Van Petegem, G. Masinelli, F. Marone, A. Salminen, A. Ganvir, K. Wasmer, R.E. Logé, Healing of keyhole porosity by means of defocused laser beam remelting: Operando observation by X-ray imaging and acoustic emission-based detection, Addit. Manuf. 79 (2024), https://doi.org/10.1016/j.addma.2023.103880.
- [2] A. du Plessis, Effects of process parameters on porosity in laser powder bed fusion revealed by X-ray tomography, Addit. Manuf. 30 (2019), https://doi.org/10.1016/ i.addma.2019.100871
- [3] N.T. Aboulkhair, N.M. Everitt, I. Ashcroft, C. Tuck, Reducing porosity in AlSi10Mg parts processed by selective laser melting, Addit. Manuf. 1 (2014) 77–86, https://doi.org/10.1016/j.addma.2014.08.001.
- [4] T.T. Roehling, R. Shi, S.A. Khairallah, J.D. Roehling, G.M. Guss, J.T. McKeown, M. J. Matthews, Controlling grain nucleation and morphology by laser beam shaping in metal additive manufacturing, Mater. Des. 195 (2020), https://doi.org/10.1016/j.matdes.2020.109071.
- [5] M. Bayat, O. Zinovieva, F. Ferrari, C. Ayas, M. Langelaar, J. Spangenberg, R. Salajeghe, K. Poulios, S. Mohanty, O. Sigmund, J. Hattel, Holistic computational design within additive manufacturing through topology optimization combined with multiphysics multi-scale materials and process modelling, Prog. Mater. Sci. 138 (2023), https://doi.org/10.1016/j.pmatsci.2023.101129.
- [6] M. Zheng, L. Wei, J. Chen, Q. Zhang, J. Li, S. Sui, G. Wang, W. Huang, Surface morphology evolution during pulsed selective laser melting: numerical and experimental investigations, Appl. Surf. Sci. 496 (2019), https://doi.org/10.1016/ iapsusc.2019.143649.
- [7] A. Plotkowski, M.M. Kirka, S.S. Babu, Verification and validation of a rapid heat transfer calculation methodology for transient melt pool solidification conditions in powder bed metal additive manufacturing, Addit. Manuf. 18 (2017) 256–268, https://doi.org/10.1016/j.addma.2017.10.017.
- [8] N. Raghavan, R. Dehoff, S. Pannala, S. Simunovic, M. Kirka, J. Turner, N. Carlson, S.S. Babu, Numerical modeling of heat-transfer and the in fl uence of process parameters on tailoring the grain morphology of IN718 in electron beam additive manufacturing, Acta Mater. 112 (2016) 303–314, https://doi.org/10.1016/j. actamat.2016.03.063.
- [9] V.K. Nadimpalli, S.A. Andersen, J.S. Nielsen, D.B. Pedersen, Considerations for interpreting in-situ photodiode sensor data in pulsed mode laser powder bed fusion, (2019).
- [10] M. Bayat, V.K. Nadimpalli, J.H. Hattel, Multiphysics simulation of thermal and fluid dynamics phenomena during the pulsed laser powder bed fusion process of 316-L steel, in: UK Heat Transfer Conference, 2022; pp. 4–6.
- [11] M. Sattari, A. Ebrahimi, M. Luckabauer, G. willem R.B.E. Römer, The effect of the laser beam intensity profile in laser-based directed energy deposition: a highfidelity thermal-fluid modeling approach, Addit. Manuf. 86 (2024), https://doi. org/10.1016/j.addma.2024.104227.
- [12] S. Shang, D. Wellburn, Y.Z. Sun, S.Y. Wang, J. Cheng, J. Liang, C.S. Liu, Laser beam profile modulation for microstructure control in laser cladding of an NiCrBSi alloy, Surf. Coat. Technol. 248 (2014) 46–53, https://doi.org/10.1016/j. surfcoat.2014.03.018.
- [13] S.N. Grigoriev, A.V. Gusarov, A.S. Metel, T.V. Tarasova, M.A. Volosova, A. A. Okunkova, A.S. Gusev, Beam shaping in laser powder bed fusion: péclet number

- and dynamic simulation, Metals 12 (2022), https://doi.org/10.3390/
- [14] R. Rothfelder, F. Huber, M. Schmidt, Influence of Beam Shape on Spatter Formation During PBF-LB/M of Ti6Al4V and Tungsten Powder. in: Procedia CIRP, Elsevier B.V, 2022, pp. 14–17, https://doi.org/10.1016/j.procir.2022.08.105.
- [15] J. Grünewald, J. Reimann, K. Wudy, Influence of ring-shaped beam profiles on spatter characteristics in laser-based powder bed fusion of metals, J. Laser Appl. 35 (2023), https://doi.org/10.2351/7.0001153.
- [16] L. Chechik, K. Schwarzkopf, R. Rothfelder, J. Grünewald, M. Schmidt, Material dependent influence of ring/spot beam profiles in laser powder bed fusion, Addit. Manuf. Lett. 9 (2024), https://doi.org/10.1016/j.addlet.2024.100211.
- [17] M. Mohammadpour, L. Wang, F. Kong, R. Kovacevic, Adjustable ring mode and single beam fiber lasers: a performance comparison, Manuf. Lett. 25 (2020) 50–55, https://doi.org/10.1016/j.mfglet.2020.07.003.
- [18] Q. Li, M. Luo, Z. Mu, A. Huang, S. Pang, Improving laser welding via decreasing central beam density with a hollow beam, J. Manuf. Process 73 (2022) 939–947, https://doi.org/10.1016/j.jmapro.2021.12.001.
- [19] P.S. Salter, M.J. Booth, Adaptive optics in laser processing, Light Sci. Appl. 8 (2019), https://doi.org/10.1038/s41377-019-0215-1.
- [20] K.S. Hansen, M. Kristiansen, F.O. Olsen, Beam Shaping to Control of Weldpool Size in Width and Depth. in: Phys Procedia, Elsevier B.V, 2014, pp. 467–476, https://doi.org/10.1016/j.phpro.2014.08.150.
- [21] W.A. Ayoola, W.J. Suder, S.W. Williams, Effect of beam shape and spatial energy distribution on weld bead geometry in conduction welding, Opt. Laser Technol. 117 (2019) 280–287, https://doi.org/10.1016/j.optlastec.2019.04.025.
- [22] W.J. Suder, S.W. Williams, Investigation of the effects of basic laser material interaction parameters in laser welding, J. Laser Appl. 24 (2012).
- [23] S. Sendino, M. Gardon, F. Lartategui, S. Martinez, A. Lamikiz, The effect of the laser incidence angle in the surface of l-pbf processed parts, Coatings 10 (2020) 1–12, https://doi.org/10.3390/coatings10111024.
- [24] K. Tsubouchi, T. Furumoto, M. Yamaguchi, A. Ezura, S. Yamada, M. Osaki, K. Sugiyama, Evaluation of spatter particles, metal vapour jets, and depressions considering influence of laser incident angle on melt pool behaviour, Int. J. Adv. Manuf. Technol. 120 (2022) 1821–1830, https://doi.org/10.1007/s00170-022-08887-w.
- [25] P. Fathi-Hafshejani, A. Soltani-Tehrani, N. Shamsaei, M. Mahjouri-Samani, Laser incidence angle influence on energy density variations, surface roughness, and porosity of additively manufactured parts, Addit. Manuf. 50 (2022), https://doi. org/10.1016/j.addma.2021.102572.
- [26] E. Li, H. Shen, L. Wang, G. Wang, Z. Zhou, Laser shape variation influence on melt pool dynamics and solidification microstructure in laser powder bed fusion, Addit. Manuf. Lett. 6 (2023), https://doi.org/10.1016/j.addlet.2023.100141.
- [27] M.J. Matthews, T.T. Roehling, S.A. Khairallah, G. Guss, S.Q. Wu, M.F. Crumb, J. D. Roehling, J.T. McKeown, Spatial Modulation of Laser Sources for Microstructural Control of Additively Manufactured Metals. in: Procedia CIRP, Elsevier B.V, 2018, pp. 607–610, https://doi.org/10.1016/j.procir.2018.08.077.
- [28] M.J. Matthews, T.T. Roehling, S.A. Khairallah, T.U. Tumkur, G. Guss, R. Shi, J. D. Roehling, W.L. Smith, B.K. Vrancken, R.K. Ganeriwala, J.T. McKeown, Controlling Melt Pool Shape, Microstructure and Residual Stress in Additively Manufactured Metals Using Modified Laser Beam Profiles. in: Procedia CIRP, Elsevier B.V, 2020, pp. 200–204, https://doi.org/10.1016/j.procir.2020.09.038.
- [29] R. Shi, S.A. Khairallah, T.T. Roehling, T.W. Heo, J.T. McKeown, M.J. Matthews, Microstructural control in metal laser powder bed fusion additive manufacturing using laser beam shaping strategy, Acta Mater. 184 (2020) 284–305, https://doi. org/10.1016/j.actamat.2019.11.053.
- [30] T.T. Roehling, S.S.Q. Wu, S.A. Khairallah, J.D. Roehling, S.S. Soezeri, M.F. Crumb, M.J. Matthews, Modulating laser intensity profile ellipticity for microstructural control during metal additive manufacturing, Acta Mater. 128 (2017) 197–206, https://doi.org/10.1016/j.actamat.2017.02.025.
- [31] (https://www.civanlasers.com/technology), Dynamic beam lasers, CIVAN Lasers, (n.d.).
- [32] E. Shekel, Y. Vidne, B. Urbach, 16kW Single Mode CW Laser with Dynamic Beam for Material Processing, in: SPIE-Intl Soc Optical Eng, 2020, p. 73, https://doi.org/ 10.1117/12.2545900.
- [33] J. Li, P. Jiang, S. Geng, J. Xiong, Numerical and experimental study on keyhole dynamics and pore formation mechanisms during adjustable-ring-mode laser welding of medium-thick aluminum alloy, Int J. Heat. Mass Transf. 214 (2023) 43, https://doi.org/10.1016/j.ijheatmasstransfer.2023.124.
- [34] Q. Hayat, P. Franciosa, G. Chianese, A. Mohan, D. Ceglarek, A. Griffiths, C. Harris, Elucidating the effect of circular and tailing laser beam shapes on keyhole necking and porosity formation during laser beam welding of aluminum 1060 using a multiphysics computational fluid dynamics approach, J. Laser Appl. 35 (2023), https://doi.org/10.2351/7.0001150.
- [35] A. Ebrahimi, M. Sattari, A. Babu, A. Sood, G.W.R.B.E. Römer, M.J.M. Hermans, Revealing the effects of laser beam shaping on melt pool behaviour in conductionmode laser melting, J. Mater. Res. Technol. 27 (2023) 3955–3967, https://doi.org/ 10.1016/j.jmrt.2023.11.046.
- [36] S.M.A. Noori Rahim Abadi, Y. Mi, F. Sikström, A. Ancona, I. Choquet, Effect of shaped laser beam profiles on melt flow dynamics in conduction mode welding, Int. J. Therm. Sci. 166 (2021), https://doi.org/10.1016/j. ijthermalsci.2021.106957.
- [37] M. Rasch, C. Roider, S. Kohl, J. Strauß, N. Maurer, K.Y. Nagulin, M. Schmidt, Shaped laser beam profiles for heat conduction welding of aluminium-copper alloys, Opt. Lasers Eng. 115 (2019) 179–189, https://doi.org/10.1016/j. optlaseng.2018.11.025.

- [38] L. Vanmunster, L. Goossens, Y. Kinds, B. Van Hooreweder, B. Vrancken, Effect of a variable laser beam profile system on productivity and surface quality of 316L stainless steel parts produced by Laser Powder Bed Fusion, CIRP Ann. 72 (2023) 121–124, https://doi.org/10.1016/j.cirp.2023.04.035.
- [39] F. Galbusera, L. Caprio, B. Previtali, A.G. Demir, The influence of novel beam shapes on melt pool shape and mechanical properties of LPBF produced Al-alloy, J. Manuf. Process 85 (2023) 1024–1036, https://doi.org/10.1016/j. imapro.2022.12.007.
- [40] R. Moore, G. Orlandi, T. Rodgers, D. Moser, H. Murdoch, F. Abdeljawad, Microstructure-based modeling of laser beam shaping during additive manufacturing, JOM 76 (2024) 1726–1736, https://doi.org/10.1007/s11837-023-0633.8
- [41] M. Bayat, W. Dong, J. Thorborg, A.C. To, J.H. Hattel, A review of multi-scale and multi-physics simulations of metal additive manufacturing processes with focus on modeling strategies, Addit. Manuf. 47 (2021), https://doi.org/10.1016/j. addma 2021 102278
- [42] J. Sundqvist, A.F.H. Kaplan, L. Shachaf, A. Brodsky, C. Kong, J. Blackburn, E. Assuncao, L. Quintino, Numerical optimization approaches of single-pulse conduction laser welding by beam shape tailoring, Opt. Lasers Eng. 79 (2016) 48–54, https://doi.org/10.1016/j.optlaseng.2015.12.001.
- [43] T. Yu, J. Zhao, Quantitative simulation of selective laser melting of metals enabled by new high-fidelity multiphase, multiphysics computational tool, Comput. Methods Appl. Mech. Eng. 399 (2022), https://doi.org/10.1016/j. cma.2022.115422
- [44] A. Chouhan, M. Hesselmann, A. Toenjes, L. Mädler, N. Ellendt, Numerical modelling of in-situ alloying of Al and Cu using the laser powder bed fusion process: a study on the effect of energy density and remelting on deposited track homogeneity, Addit. Manuf. 59 (2022), https://doi.org/10.1016/j. addma.2022.103179.
- [45] L. Yao, S. Huang, U. Ramamurty, Z. Xiao, On the formation of "Fish-scale" morphology with curved grain interfacial microstructures during selective laser melting of dissimilar alloys, Acta Mater. 220 (2021) 117331, https://doi.org/10.1016/j.actamat.2021.117331.
- [46] V.E. Küng, R. Scherr, M. Markl, C. Körner, Multi-material model for the simulation of powder bed fusion additive manufacturing, Comput. Mater. Sci. 194 (2021), https://doi.org/10.1016/j.commatsci.2021.110415.
- [47] J. Jakumeit, G. Zheng, R. Laqua, S.J. Clark, J. Zielinski, J.H. Schleifenbaum, P. D. Lee, Modelling the complex evaporated gas flow and its impact on particle spattering during laser powder bed fusion, Addit. Manuf. 47 (2021) 102332, https://doi.org/10.1016/j.addma.2021.102332.
- [48] X. Li, C. Zhao, T. Sun, W. Tan, Revealing transient powder-gas interaction in laser powder bed fusion process through multi-physics modeling and high-speed synchrotron x-ray imaging, Addit. Manuf. 35 (2020) 101362, https://doi.org/ 10.1016/j.addma.2020.101362.
- [49] H. Chen, W. Yan, Spattering and denudation in laser powder bed fusion process: Multiphase flow modelling, Acta Mater. 196 (2020) 154–167, https://doi.org/ 10.1016/j.actamat.2020.06.033.
- [50] M. Bayat, J.H. Hattel, High-fidelity numerical modelling of cold spatter formation during laser powder bed fusion of 316-1 stainless steel, in: C. Sommitsch, N. Enzinger, P. Mayr (Eds.), The 14th International Seminar "Numerical Analysis of Weldability." Graz. 2022.
- [51] T.U. Tumkur, T. Voisin, R. Shi, P.J. Depond, T.T. Roehling, S. Wu, M.F. Crumb, J.D. Roehling, G. Guss, S.A. Khairallah, M.J. Matthews, Nondiffractive beam shaping for enhanced optothermal control in metal additive manufacturing, 2021. (https://www.science.org/)
- [52] M. Bayat, A. Thanki, S. Mohanty, A. Witvrouw, S. Yang, J. Thorborg, N.S. Tiedje, J. H. Hattel, Keyhole-induced porosities in laser-based powder bed fusion (L-PBF) of Ti6Al4V: high-fidelity modelling and experimental validation, Addit. Manuf. 30 (2019), https://doi.org/10.1016/j.addma.2019.100835.
- [53] M. Bayat, V.K. Nadimpalli, D.B. Pedersen, J.H. Hattel, A fundamental investigation of thermo-capillarity in laser powder bed fusion of metals and alloys, Int. J. Heat. Mass Transf. 166 (2021), https://doi.org/10.1016/j. ijheatmasstransfer.2020.120766.
- [54] G. Parivendhan, M.C. Smith, T.F. Flint, Numerical Modelling Approaches for Simulating Powder Bed Fusion Processes Fracture and Fatigue Mechanics and Mechanisms of Polymer Fibre Composites View project The finite volume method for solid mechanics View project, (n.d.). https://doi.org/10.13140/RG.2.2.24
- [55] T.F. Flint, M.J. Anderson, V. Akrivos, M.J. Roy, J.A. Francis, A. Vasileiou, M. C. Smith, A fundamental analysis of factors affecting chemical homogeneity in the laser powder bed fusion process, Int. J. Heat. Mass Transf. 194 (2022), https://doi.org/10.1016/j.ijheatmasstransfer.2022.122985.
- [56] M. Bayat, S. Mohanty, J.H. Hattel, Multiphysics modelling of lack-of-fusion voids formation and evolution in IN718 made by multi-track/multi-layer L-PBF, Int. J. Heat. Mass Transf. 139 (2019) 95–114, https://doi.org/10.1016/j. ijheatmasstransfer.2019.05.003.
- [57] W. Tan, N.S. Bailey, Y.C. Shin, Investigation of keyhole plume and molten pool based on a three-dimensional dynamic model with sharp interface formulation, J. Phys. D Appl. Phys. 46 (2013), https://doi.org/10.1088/0022-3727/46/5/ 055501.
- [58] R. Lin, H. ping Wang, F. Lu, J. Solomon, B.E. Carlson, Numerical study of keyhole dynamics and keyhole-induced porosity formation in remote laser welding of Al alloys, Int. J. Heat. Mass Transf. 108 (2017) 244–256, https://doi.org/10.1016/j. ijheatmasstransfer.2016.12.019.
- [59] A. Charles, M. Bayat, A. Elkaseer, L. Thijs, J.H. Hattel, S. Scholz, Elucidation of dross formation in laser powder bed fusion at down-facing surfaces: phenomenon-

- oriented multiphysics simulation and experimental validation, Addit. Manuf. 50 (2022), https://doi.org/10.1016/j.addma.2021.102551.
- [60] O. Zinovieva, V. Romanova, A. Zinoviev, O. Nekhorosheva, R. Balokhonov, Elastic properties of additively manufactured steel produced with different scan strategies, Int. J. Mech. Sci. 244 (2023) 108089, https://doi.org/10.1016/j. ijmecsci.2022.108089.
- [61] O. Zinovieva, A. Zinoviev, V. Romanova, R. Balokhonov, Three-dimensional analysis of grain structure and texture of additively manufactured 316L austenitic stainless steel, Addit. Manuf. 36 (2020) 101521, https://doi.org/10.1016/j. addma.2020.101521.
- [62] O. Zinovieva, A. Zinoviev, V. Ploshikhin, Three-dimensional modeling of the microstructure evolution during metal additive manufacturing, Comput. Mater. Sci. 141 (2018) 207–220, https://doi.org/10.1016/j.commatsci.2017.09.018.
- [63] J. Zhang, L. Wu, L. Zhang, L. Meng, Phase field simulation of dendritic microstructure in additively manufactured titanium alloy, Met. Powder Rep. 74 (2021)
- [64] D. Liu, Y. Wang, Mesoscale multi-physics simulation of rapid solidification of Ti-6Al-4V alloy, Addit. Manuf. 25 (2019) 551–562, https://doi.org/10.1016/j. addma 2018 12 005
- [65] S. Sahoo, K. Chou, Phase-field simulation of microstructure evolution of Ti-6Al-4V in electron beam additive manufacturing process, Addit. Manuf. 9 (2016) 14–24, https://doi.org/10.1016/j.addma.2015.12.005.
- [66] O. Zinovieva, A. Zinoviev, V. Ploshikhin, Three-dimensional modeling of the microstructure evolution during metal additive manufacturing, Comput. Mater. Sci. 141 (2018) 207–220, https://doi.org/10.1016/j.commatsci.2017.09.018.
- [67] Y. Wang, S. Chu, Z. Wang, J. Li, J. Wang, On Ti6Al4V microsegregation in electron beam additive manufacturing with multiphase-field simulation coupled with thermodynamic data, Acta Metall. Sin. Engl. Lett. 35 (2022) 425–438, https://doi. org/10.1007/s40195-021-01318-x.
- [68] M.J. Bermingham, S.D. McDonald, M.S. Dargusch, D.H. St. John, Grain-refinement mechanisms in titanium alloys, J. Mater. Res. 23 (2008) 97–104, https://doi.org/ 10.1557/jmr.2008.0002.
- [69] W. Wang, P.D. Lee, M. McLean, A model of solidification microstructures in nickel-based superalloys: predicting primary dendrite spacing selection, Acta Mater. 51 (2003) 2971–2987, https://doi.org/10.1016/S1359-6454(03)00110-1.
- [70] Y.C. Wu, C.H. San, C.H. Chang, H.J. Lin, R. Marwan, S. Baba, W.S. Hwang, Numerical modeling of melt-pool behavior in selective laser melting with random powder distribution and experimental validation, J. Mater. Process Technol. 254 (2018) 72–78, https://doi.org/10.1016/j.jmatprotec.2017.11.032.
- [71] Y.S. Lee, W. Zhang, Modeling of heat transfer, fluid flow and solidification microstructure of nickel-base superalloy fabricated by laser powder bed fusion, Addit. Manuf. 12 (2016) 178–188, https://doi.org/10.1016/j.addma.2016.05.003.
- [72] N. Kouraytem, X. Li, W. Tan, B. Kappes, A.D. Spear, Modeling process structure property relationships in metal additive manufacturing: a review on physics-driven versus data-driven approaches, J. Phys. Mater. 4 (2021).
   [73] M. Zheng, L. Wei, J. Chen, Q. Zhang, C. Zhong, X. Lin, W. Huang, A novel method
- [73] M. Zheng, L. Wei, J. Chen, Q. Zhang, C. Zhong, X. Lin, W. Huang, A novel method for the molten pool and porosity formation modelling in selective laser melting, Int. J. Heat. Mass Transf. 140 (2019) 1091–1105, https://doi.org/10.1016/j. iiheatmasstransfer.2019.06.038.
- [74] C. Tang, J.L. Tan, C.H. Wong, A numerical investigation on the physical mechanisms of single track defects in selective laser melting, Int. J. Heat. Mass Transf. 126 (2018) 957–968, https://doi.org/10.1016/j. iiheatmasstransfer 2018 06 073
- [75] C. Tang, K.Q. Le, C.H. Wong, Physics of humping formation in laser powder bed fusion, Int. J. Heat. Mass Transf. 149 (2020), https://doi.org/10.1016/j. iiheatmasstransfer 2019 119172
- [76] W.E. King, H.D. Barth, V.M. Castillo, G.F. Gallegos, J.W. Gibbs, D.E. Hahn, C. Kamath, A.M. Rubenchik, Observation of keyhole-mode laser melting in laser powder-bed fusion additive manufacturing, J. Mater. Process Technol. 214 (2014) 2915–2925, https://doi.org/10.1016/j.jmatprotec.2014.06.005.
- [77] W.E. Alphonso, M. Baier, S. Carmignato, J.H. Hattel, M. Bayat, On the possibility of doing reduced order, thermo-fluid modelling of laser powder bed fusion (L-PBF) – assessment of the importance of recoil pressure and surface tension, J. Manuf. Process Accept. (2023).
- [78] T.N. Le, Y.L. Lo, Effects of sulfur concentration and Marangoni convection on melt-pool formation in transition mode of selective laser melting process, Mater. Des. 179 (2019) 107866, https://doi.org/10.1016/j.matdes.2019.107866.
- [79] K.Q. Le, C. Tang, C.H. Wong, On the study of keyhole-mode melting in selective laser melting process, Int. J. Therm. Sci. 145 (2019), https://doi.org/10.1016/j. iithermalsci.2019.105092
- [80] M. Bayat, S. Mohanty, J.H. Hattel, A systematic investigation of the effects of process parameters on heat and fluid flow and metallurgical conditions during laser-based powder bed fusion of Ti6Al4V alloy, Int. J. Heat. Mass Transf. 139 (2019) 213–230. https://doi.org/10.1016/j.iijheatmasstransfer.2019.05.017
- (2019) 213–230, https://doi.org/10.1016/j.ijheatmasstransfer.2019.05.017.
   [81] S.A. Khairallah, A.T. Anderson, A. Rubenchik, W.E. King, Laser powder-bed fusion additive manufacturing: Physics of complex melt flow and formation mechanisms of pores, spatter, and denudation zones, Acta Mater. 108 (2016) 36–45, https://doi.org/10.1016/j.actamat.2016.02.014.
- [82] C. Qiu, C. Panwisawas, M. Ward, H.C. Basoalto, J.W. Brooks, M.M. Attallah, On the role of melt flow into the surface structure and porosity development during selective laser melting, Acta Mater. 96 (2015) 72–79, https://doi.org/10.1016/j. actamat.2015.06.004.
- [83] C. Chattopadhyay, S. Sangal, K. Mondal, A relook at the preferred growth direction of the solid-liquid interface during solidification of pure metals, Acta Mater. 58 (2010) 5342–5353, https://doi.org/10.1016/j.actamat.2010.06.009.

- [84] H. Wang, Y. Wang, X. Li, W. Wang, X. Yang, Influence of assembly gap size on the structure and properties of SUS301L stainless steel laser welded lap joint, Materials 14 (2021) 996, https://doi.org/10.3390/ma14040996.
- [85] Z. Jiang, X. Chen, H. Li, Z. Lei, Y. Chen, S. Wu, Y. Wang, Grain refinement and laser energy distribution during laser oscillating welding of Invar alloy, Mater. Des. 186 (2020) 108195, https://doi.org/10.1016/J.MATDES.2019.108195.
- [86] R. Moore, G. Orlandi, T. Rodgers, D. Moser, H. Murdoch, F. Abdeljawad, Microstructure-based modeling of laser beam shaping during additive manufacturing, JOM 76 (2024) 1726–1736, https://doi.org/10.1007/s11837-023-06363-8.
- [87] M.H. Nasab, G. Masinelli, L. Schlenger, S. Van Petegem, P. Scherrer, K. Wasmer, A. Ganvir, A. Salminen, F. Aymanns, F. Marone, V. Pandiyan, S. Goel, Operando X-Ray imaging of stochastic inter-regime instabilities in laser melting processes: direct evidence of acoustic emission signatures, (2023). https://doi.org/10.21203/rs.3.rs-2607808/v1.
- [88] M. Hamidi Nasab, G. Masinelli, C. de Formanoir, L. Schlenger, S. Van Petegem, R. Esmaeilzadeh, K. Wasmer, A. Ganvir, A. Salminen, F. Aymanns, F. Marone, V. Pandiyan, S. Goel, R.E. Logé, Harmonizing sound and light: X-ray imaging unveils acoustic signatures of stochastic inter-regime instabilities during laser melting, Nat. Commun. 14 (2023), https://doi.org/10.1038/s41467-023-43371-3.